Understanding degradation mechanisms in spray-coated alternating silicon-carbon thin films as anodes for lithium-ion batteries

Tilo Held [a,b,1,*] , Wiebke Hagemeier [a,1] , Daniel Leykam [a], Christina Roth [a,b]

[a] *University of Bayreuth, Chair of Electrochemical Process Engineering, Universitätsstraße 30, Bayreuth 95447, Germany*
[b] *Bavarian Center for Battery Technology (BayBatt), Weiherstraße 26, Bayreuth 95448, Germany*

ARTICLE INFO

ABSTRACT

Silicon's high specific capacity makes it one of the most promising new materials for anode applications. However, its performance is limited by its cycling stability. Approaches to remedy the various degradation mechanisms (pulverization, delamination and excessive solid electrolyte interphase (SEI) formation) include the use of silicon-carbon (Si/C) composites or the manufacturing of thin layers. In this study, two approaches were combined by producing alternating silicon and reduced graphene oxide (rGO) layers using a spray-coating process. This allowed us to draw important conclusions regarding the relationship between the silicon layer thickness and the total silicon content of the electrode and the resulting degradation behavior. Moreover, this study examined the suitability of prelithiated polyacrylic acid (LiPAA) as binder for spray-coating and its electrochemical performance. Using X-ray photoelectron spectroscopy (XPS), X-ray diffraction (XRD) and optical microscopy cross-sections, electrochemical impedance spectroscopy (EIS), galvanostatic intermittent titration technique (GITT) and galvanostatic cycling, it could be demonstrated that the silicon layer thickness is a limiting factor for a stable cycling performance and can therefore result in an inhomogeneous charge distribution within the electrode. Understanding the correlation between the layer morphology and degradation behavior is essential to allow for the realization of composite electrodes with a high capacity retention.

1. Introduction

According to current research, graphite-based anode materials continue to dominate in lithium-ion batteries (LIB) with a theoretical capacity of 372 mAh g^{-1}. Silicon, on the other hand, offers an enormous potential for improvement with its maximum capacity of 3579 mAh g^{-1}, but also provides new challenges [1,2]. A major disadvantage of pure silicon electrodes is the low electrical conductivity (10^{-4} S m^{-1}) of the material itself, which causes their less favorable fast charging behavior compared to graphitic electrodes [3,4]. To address this disadvantage, the use of silicon-carbon (Si/C) composite electrodes is currently an active field of research. Silicon-carbon composites possess the required conductivity and subsequently increased storage capacity [5]. Nevertheless, the process of silicon lithiation is responsible for a non-uniform volume expansion of up to 300 %, leading to mechanical stress within the electrode layer. Furthermore, the two-step expansion (1st: Si + 2Li$^+$ + 2e$^-$ → Li$_{2.0}$Si; 2nd: Li$_{2.0}$Si + 1.75Li$^+$ + 1.75e$^-$ → Li$_{3.75}$Si) causes the amorphization of the pristine crystalline lattice. This structural change causes further degradation of the material, which can hardly be avoided [2,6].

This issue is particularly prevalent when microcrystalline silicon particles are selected, resulting in pulverization and electrical isolation of the cracked particles. In addition, delamination of the current collector is a significant problem, using microscale particles or nanoscale particles in Si-rich composite formulations [7,8]. However, since it is cost effective to select cheap, crystalline, microscale Si particles, these issues need to be overcome. One promising solution is to partially lithiate the Si particles [6,9]. This reduces the degradation of silicon, which is particularly pronounced when cycling over the 0–30 % SoC range [10]. A disadvantage of this strategy, apart from the lower electrical conductivity due to the higher silicon content in the electrode, however, is the comparatively high proportion of electrochemically inactive material, which adds to the weight, while not contributing to the electrochemical performance.

An alternative approach involves implementing nanoscale Si particles with a critical particle size below 150 nm. At this scale, the

---

nanoparticles are not yet subject to pulverization due to the mechanical stress caused by the high volume expansion [11]. A full lithiation of the particles furthermore allows for the utilization of the entire electrode capacity. However, the high surface-to-volume ratio of amorphized nanoparticles leads to progressive degradation originating from a continuously growing passivation layer. To face this issue, it is possible to create specifically-structured composite materials by encapsulating individual nanoscale particles or forming nanostructured microparticles [12–17]. Yet, such sophisticated synthesis routes require significant time and monetary investments, presenting considerable challenges when scaling up to industrial levels. Another method for enhancing cycling stability involves stabilizing the solid electrolyte interphase (SEI), which is primarily composed of degradation products from the electrolyte and conducting salt [18,19], by specifically selected additives and hampering its further growth.

If the contact area between Si nanoparticles is to be reduced, one way forward could be the fabrication of dimensionally-restricted layered silicon-carbon composite electrodes, e.g. produced by magnetron sputtering of individual layers [20–22]. This technique can mitigate the direct interaction between the Si surface and the electrolyte [23] by covering the silicon layers with carbonaceous buffer material in a controlled manner. Such an intricate structure will reduce the excessive SEI formation on the silicon surface significantly, but is limited by the maximum layer thickness, which leads to the pulverization of the Si layer, akin to the degradation of microparticles [24].

To address and overcome these issues, this study aims to synthesize alternating Si/C thin films based on silicon nanoparticles. The silicon and carbon layers are deposited in an alternating sequence via a spray-coating process. In contrast to methods such as magnetron sputtering or chemical vapor deposition, spray-coating relies on a solvent-based process. Another difference is the final electrode composition and its morphology. A thin-film electrode produced using the process described here has a binder content of 15 or 25 wt.%. In addition, conductivity additives can be incorporated into the ink. Compared to binder-free electrodes, which are the product of a PVD or CVD process, these contain only active material. Another advantage of the spray-coating process is the deposition rate, which is several orders of magnitude higher (e.g. 0.2 nm min^{-1} for carbon, 4.4 nm min^{-1} for silicon vs. > 1 μm min^{-1} for the presented method) [25]. The increased deposition rate is accompanied by a reduced processing time and a simplified scalability to an industrial scale for continuous production. In comparison to the more time-consuming and resources-intensive wet chemical syntheses [26–29], it results in the same material combination but a completely different electrode structure. To the best of our knowledge, only two other groups reported a similar approach before [23,30]. However, in these works polyvinylidene fluoride (PVDF)-based binder systems have been employed, which should be avoided due to their toxicity. Furthermore, various research groups have identified the advantages of LiPAA as a binder system for silicon-containing electrodes compared to, for example, PVDF [31,32], PVA [32] Na-CMC [33] and non-lithiated PAA [34]. We evaluated LiPAA as alternative to today's state of the art binders with respect to its applicability in the spray-coating process, as spray-coating is suitable for industrial applications in views of rapid film deposition, facile automation, and easy scale-up. Furthermore, the μm-thick films consisting of nm-sized Si-particles are expected to feature an improved porosity and with respect to this shorter diffusion pathways and a higher conductivity [23]. In this context, the carbon matrix consisting of reduced graphene oxide (rGO) and acetylene carbon black (ACB), serves as a mediator for the electric and ionic conductivity of the entire silicon layer. This is in contrast to typical approaches utilizing the carbon matrix embedding the individual silicon particles in the multilayer graphene [29,35]. The spherical structure of the rGO multilayers is not employed for the purpose of encapsulating silicon; rather, it is utilized to ensure the electron and ion conductivity of the single silicon layers, even if entire areas of the electrode expand by several 100 % due to amorphization and alloy

formation. Particular consideration was given to the number of silicon interlayers and the varying silicon contents in the individual layers as well as in the composite electrodes as a whole. By elucidating the influence of these parameters, conclusions can be drawn regarding alterations in morphology.

2. Experimental

2.1. Material and ink preparation

The synthesis of reduced graphene oxide (rGO) was carried out using a two-step procedure, which is explained in detail in the publication by Müllner et al. using graphene oxide (GO) (EXG R98 300, *Graphit Kropfmühl*) as a starting material [36]. The material was put into a four-neck flask and heated under argon atmosphere using a heating mantle (PILZ, *Heraeus*) to 400 °C mantle temperature. At this temperature the thermal exfoliation in combination with a large volumetric expansion takes place. This material was further reduced at 700 °C in Ar for 2 h (heating rate: 10 °C min^{-1}) with subsequent cooling of the rGO to room temperature in a tube furnace (*Carbolite*). The reduced graphene oxide was then ball milled (Simoloyer CM01, *Zoz GmbH*) at 1500 rpm for one hour. The rotor-stator system as well as the grinding balls (material to grinding ball weight ratio 1:20) were made of polyether ether ketone (PEEK). In this work, one batch of synthesized rGO was used for all electrodes investigated. Therefore, a constant elemental composition (e. g., C/O ratio) can be assumed for all electrodes shown.

A binder system based on lithium polyacrylic acid (LiPAA) was used. To prepare the prelithiated LiPAA binder, a 35 wt.% aqueous polyacrylic acid solution (Sigma Aldrich) was diluted to a 10 wt.% solution. Lithium hydroxide (LiOH, *Thermo Scientific*) was then added to it until a neutral pH of 7 was obtained.

The carbon and the silicon containing inks were prepared in two different ways due to the different behavior of the particles. The conductive agent acetylene carbon black (ACB, *Strem Chemicals*) was added to the ink with rGO for comparability with further carbon-based inks. The solid content of the unprocessed ink was 10 wt.%. In the dried layer, a ratio of 75 wt.% rGO, 10 wt.% ACB and 15 wt.% binder was used. The silicon nanoparticles (100 nm, *Thermo Scientific*) were deagglomerated in a water/isopropanol solution in a mixing ratio of 3:2 (wt/wt) (*VWR Chemicals*) using a sonotrode (Sonifier W-450 D, *Branson Digital*). The binder was added to the dispersion after deagglomeration. The solution was homogenized in an ultrasonic bath (P60 H, *Elma*) for 10 min. The solid content in the silicon ink was 4 wt.%. In the dried layer, a ratio of 75 wt.% silicon and 25 wt.% binder was used.

2.2. Spray-coating procedure

The inks produced in this way were then applied alternately to the copper current collector (20 μm, H+S Präzisionsfolien GmbH) as shown in Fig. 1.

The spray-coating process was carried out manually using an airbrush gun (Airbrush 206430, *Conrad Electronic*). Nitrogen was used as the carrier gas for aerosol formation. The gas flows perpendicular to the copper substrate from the gas nozzle over the material outlet, creating a negative pressure which draws the ink to the nozzle. The ink is finely nebulized by the gas stream and applied to the substrate as an aerosol. A polytetrafluoroethylene (PTFE) stencil was used to spray an exact area of 30×60 mm^2. The spray gun was moved over the sample area at a speed of 5 cm s^{-1}, achieving a deposition rate of around 1 mg s^{-1} for silicon and 2 mg s^{-1} for rGO. The different deposition rates of the two slurries can be attributed to the different solids contents due to the varying processability. After each spraying step, the electrodes were weighed to ensure uniform electrode loading. In order to ensure complete and fast evaporation of the solvent after each sprayed layer and a satisfactory process speed, the copper substrate was heated to 70 °C on a heating plate. At this temperature, the water evaporates to ensure a
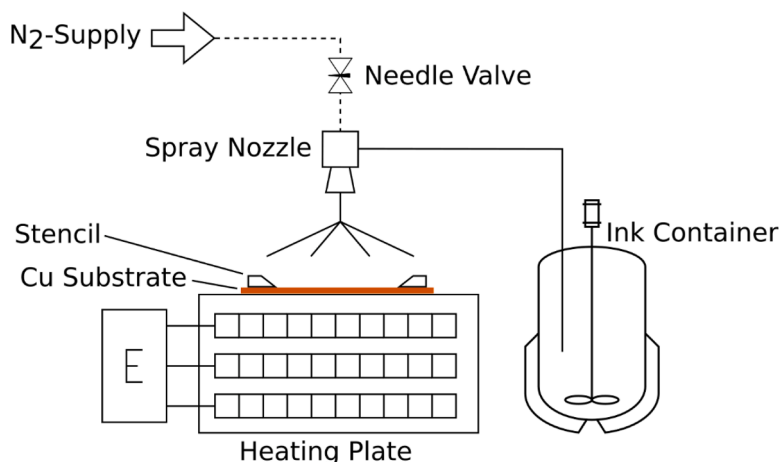
Fig. 1. Schematic flowsheet of the spray-coating process. The ink container is likewise filled with a mixture of rGO, LiPAA, ACB and a water/isopropanol mixture for the carbon ink or Si, LiPAA and a water/isopropanol mixture for the silicon ink.

satisfactory process speed. Nevertheless, the temperature is low enough to avoid sudden evaporation, which causes cracking of the electrode. Consequently, the individual layers are applied in a successive manner, with intermediate drying stages. The difference in particle size between μm-sized rGO and nanoscale silicon results in individual rGO layers being considerably thicker than the individual silicon layers for a single spraying step. To underline this difference once again, SEM/EDS images of the respective individual components (GO, rGO, nm-Si and ACB) of the electrodes are included in the SI in Fig. 1. However, these are denser due to their spherical shape. The minimum layer thickness is limited to at least 1 μm for silicon and rGO due to the experimental setup, the particle size of the individual particles and the fact that at least 2 to 3 spraying steps are required for a continuous layer. The influence of packing density was minimized by maintaining consistent conditions, i. e. the duration and number of individual spraying operations per layer and a constant ink composition. We have included the area specific mass loading of the electrodes examined in Table 1 of the SI. It is not possible to constantly adjust the porosity and with that the mass loading due to the different particle sizes of rGO and silicon. The porosity decreases and the mass loading increases with increasing silicon content.

2.3. Half-cell assembly and cycling

The assembly of the coin-cell-type half-cells (Swagelok cell) was carried out in an argon-filled glove box (O_2 content < 5 ppm, H_2O

content < 1 ppm). The anodes produced have a diameter of 12 mm and were punched using a punching iron (El-Cut from *El Cell GmbH*). The electrodes were dried in a tube furnace at 110 °C for 12 h in Ar atmosphere before being placed in the glove box. Whatman GF/C glass microfiber filters (125 μm, *Sigma Aldrich*) with a diameter of 12.5 mm were used as separators. A 0.6 mm thick lithium sheet with a diameter of 12 mm (*Goodfellow GmbH*) was used as the counter electrode. For each cell, 150 μl of electrolyte consisting of fluoroethyl carbonate (FEC) and diethyl carbonate (DEC) in a ratio of 1:4 (v/v) with 1 mol of lithium hexafluorophosphate ($LiPF_6$) (*E-Lyte Innovations*) was used. In this type of setup, a nickel plate (d = 12 mm, h = 500 μm; HMW Hauner) and a steel spring (EN-material number: 1.4310, *Gutekunst Federn*) were positioned on the lithium counter electrode to ensure a constant contact pressure of 0.05 MPa.

The cells underwent galvanostatic cycling using a CTS Lab battery tester (*BaSyTec GmbH*). Cycling was performed at a C-rate of C/10, with the voltage range maintained at 0.01 to 1.5 V for 50 cycles, corresponding to 100 mA g^{-1} current density. Afterwards, a C-rate variation was performed for 5 cycles each with C/5, C/2, C/1 and finally C/10 again. Each cell type was measured up to four times and a mean value with standard deviation was calculated. To be able to draw conclusions regarding the voltage-dependent capacity distribution, dq/dU characteristics are generated using an in-house built script for data processing described in detail in a former publication [37]. This routine applies an unconditionally stable smoothing according to a one-dimensional

Table 1

Summary of the physico-chemical properties of ACB, rGO, Si, SirGO@LiPAA from CHNS, BET, XPS, pull-off adhesion and EIS analyses.

	Properties	Unit	ACB	rGO	Si	Si/rGO/ACB[b]	SirGO@LiPAA
CHNS	C content	at.%	99.6	79.6	-	-	-
	O content		0.0	10.2	-	-	-
	H content		0.3	10.0	-	-	-
	N content		0.1	0.1	-	-	-
	S content		0.0	0.1	-	-	-
BET	Surface area	m^2 g^{-1}	71	179	38	119	-
XPS	C=C sp^2	at.%	39	31.9	-	28.5	26.4
C1s	C-C, C-H		34	34.5	-	46.5	43.3
	C-O		13	8.3	-	6.0	10.9
	C=O		15	8.7	-	6.2	2.4
	O-C=O		0.0	6.3	-	5.1	9.0
	Pi-Pi		0.0	9.6	-	7.7	8.0
XPS	Si	at.%	-	-	21.2	40.9	22.5
Si2p	Si^{+1}		-	-	19.5	17.6	12.4
	Si-O		-	-	59.3	41.5	65.2
Pull-off adhesion	IPF[a]	MPa	-	-	-	-	8.7[c]
EIS	conduc-tivity	S m^{-1}	387[b]	20[b]	<10^{-4b}	11[b]	0.6[c]

[a] Interfacial peeling strength, measured [b]as powder, [c]on a Cu-current collector as electrode.

diffusion pulse by exploiting the semi-implicit Crank-Nicolson method [37]. To examine the Li$^+$ diffusion depending on the degree of lithiation of the electrodes, galvanostatic intermittent titration technique (GITT) was used. The applied current corresponds to a C/10 rate and was maintained for 10 min as well as a rest time of 10 min. The theoretical capacity was calculated based on the weight of the active material content in each individual layer. For the carbon-based interlayers, the theoretical capacity of graphite (LiC$_6$, 372 mAh g^{-1}) has been utilized for calculation, while for the silicon-based interlayers the entirely lithiated phase at room temperature Li$_{3.75}$Si (3579 mAh g^{-1}) has been considered.

2.4. Materials and electrode characterization

To examine the specific surface area, the N$_2$ physisorption via the Brunauer-Emmet-Teller method (BET) was used with Belsorp Mini X from *Microtrac Retsch*. The X-ray diffractometer (XRD, X'Pert MPD type: PW 3040/00, *Philips Analytical*) is used for the characterization of the crystal structure of the investigated powders and electrodes. The diffraction patterns were acquired with Cu K$_\alpha$ radiation at scattering angles in the range of $10° − 90°$ 2θ with a step size of 0.02° at a scanning speed of 10 s at room temperature in Bragg-Brentano configuration. A scanning electron microscope (SEM, Ultra plus, Zeiss, Jena, Germany) was used to determine the surface properties of the individual materials and the electrodes. To identify the element distribution of the silicon particles in the rGO matrix and analyze the layer thickness pristine and post-mortem, energy dispersive X-ray analyses (EDS, NS7, Thermo Fisher Scientific, Waltham, MA, USA) were carried out on selected samples. The data was post treated in terms of background subtraction and K$_{\alpha2}$ stripping via the software HighScore v.4.8 *(Malvern Panalytical B.V.*, Netherlands). The X-ray photoelectron spectroscopy (XPS) analysis was carried out with a VersaProbe III Scanning XPS Mircoprobe (*Physical Electronics, Inc.*) equipped with a monochromized Al K$_\alpha$ X-ray excitation source (1486.74 eV), with a beam diameter of 100 μm and a pass energy of 26 eV for survey scans and 224 eV for high-resolution, respectively. The surface structure is investigated for the C 1s, O 1s and Si 2p edges dependent on the presence of the respective element. The XPS studies were carried out with the latest fityk evaluation software v1.3.1. Before fitting, the C 1s signal was set to 284.8 eV for charge correction of the raw data. The Fourier transform infrared (FT-IR) spectrometry (Tensor 27, *Bruker*) was performed with attenuated total reflection (Platinum-ATR) to detect the asymmetric vibrations of molecular bonds in the investigated materials. Light microscopy (BX60M, *Olympus*) was used to investigate cross sections of the electrodes before and after cycling. Therefore, the electrodes were embedded in epoxy resin and grinded (grit size: 180–2000) and polished with diamond suspension (1 μm) with a RotoPol-31 from Struers. The embedding of the electrode in resin, followed by grinding, has been observed to result in the release of particles and particle agglomerates. This process has been found to lead to the formation of fractures or voids which could incorrectly indicate an inhomogeneous layer structure. For the pull-off adhesion test, the samples were glued to a steel plate with 2-component adhesive (epoxy glue EA9466, *Loctite*). Dollys with a diameter of 10 mm were glued on the electrode. The adhesive was hardened for one hour at 110 °C. After that, the dollies were peeled off with a pull-off rate of 1 MPa s^{-1} with the PosiTest AT-A from *mtv Messtechnik*. The electrical conductivities were measured using galvanostatic impedance spectroscopy (GEIS) with a Reference 600 (*Gamry*). The measurements were taken at a current of 0.05 mA over a frequency range of 1.000 to 10 Hz. Thereby a compression of 0.5 MPa was applied using a universal testing machine (Instron Series 5569).

3. Results and discussion

The focus of our study is the variation of number and thickness of the Si interlayers and will be treated and discussed separately below. The

electrodes were characterized in terms of composition and morphology through the use of X-ray diffraction (XRD), elemental analysis (CHNS-O), as well as N2 physisorption (BET) and X-ray photoelectron spectroscopy (XPS) measurements. Scanning electron microscope (SEM) and light microscopic analyses of the cross-sections of pristine and post-mortem electrodes were carried out, with a focus on the observed changes at the micro- and macrostructural levels. This was complemented by energy dispersive X-ray spectroscopic (EDS) analysis. Electrochemical characterization was performed using electrochemical impedance spectroscopy (EIS), the Galvanostatic Intermittent Titration Technique (GITT), and galvanostatic coulometry. A post-mortem analysis was conducted with the objective of identifying changes in layer parameters, including thickness, number, and total amount of Si, and their impact on the electrochemical properties of the individual layer and the electrode.

3.1. Interaction of binder and active material surface functionalities

A decisive factor in producing both mechanically and electrochemically stable electrodes is the selection of a suitable binder system. Various research groups have identified the advantages of LiPAA as a binder system for silicon-containing electrodes compared to, for example, PVDF [31,32], PVA [32] Na-CMC [33] and non-lithiated PAA [34]. The reduced graphene oxides used here do not have a perfect graphitic structure, but feature defects in the form of voids and polar surface groups depending on their respective post-reduction treatment. Silicon nanoparticles also have a surface oxide layer that interacts with the used binder system. The advantages of LiPAA over these comparative systems include increased chemical and mechanical stability, which is reflected in improved electrochemical performance and the avoidance of the use of NMP as a solvent. LiPAA forms the strongest interaction forces between the active material and the binder due to the hydroxyl and carboxylic acid groups present [31,32,38]. To be able to explain the electrochemical behavior of the composites and their interaction with the chosen binder, the physico-chemical properties of the starting materials and electrodes were examined first.

Table 1 summarizes the results of the CHNS, BET and XPS analyses of the individual starting materials, the adhesive strength of the composite electrodes and their electrical conductivity.

3.1.1. CHNS elemental, FTIR and XPS analysis

According to Table 1, the rGO material of the interlayer has an oxygen content of 10.2 at.% and a hydrogen content of 10.0 at.% which results in its strong interaction with the different binders, due to the high amount of remaining functional groups. In contrast, acetylene carbon black (ACB) has a high carbon content of > 99 at.% with only minor impurities, as common for commercial conductive additives. Considering the BET analysis, it is found that the specific surface area of 179 m^2 g^{-1} for rGO (pristine GO: 37 m^2 g^{-1}) is significantly higher than for ACB with 71 m^2 g^{-1}. This finding can be assigned to its expanded structure formed during the reduction process as well as to the removal of surface functional groups, which can be seen in the SEM images in Fig. S1 [37].

The investigated silicon nanoparticles have a high fraction of surface oxides, as revealed by the analysis of their Si 2p spectra (Si-O 59.3 at.%). These surface oxides can interact with the polar entities of the used binder [39]. Since polyacrylic acid (PAA) contains a higher ratio of carboxy groups, it is the preferred binder for silicon-containing electrodes [40]. In addition, the high fraction of -COOH in acrylic acid leads to strong adhesion and therefore a lower tendency of SEI formation [41, 42]. Based on the analysis of the C1s excitation of rGO, as detailed in Supplementary Information S1, a considerable proportion of functional, oxygen-containing groups such as C-O (8.3 at.%), C=O (8.7 at.%), and COOH (6.3 at.%) remains within the carbon lattice after thermal exfoliation. Conversely, the fraction of non-polar groups is significantly lower, resulting in fewer bonds to the non-polar graphitic surfaces. However, rGO has a high amount of remaining surface functionalities,

which lead to a more polar surface compared to graphite. Therefore, it can be assumed that good adhesion with the binder will also occur in this specific case.
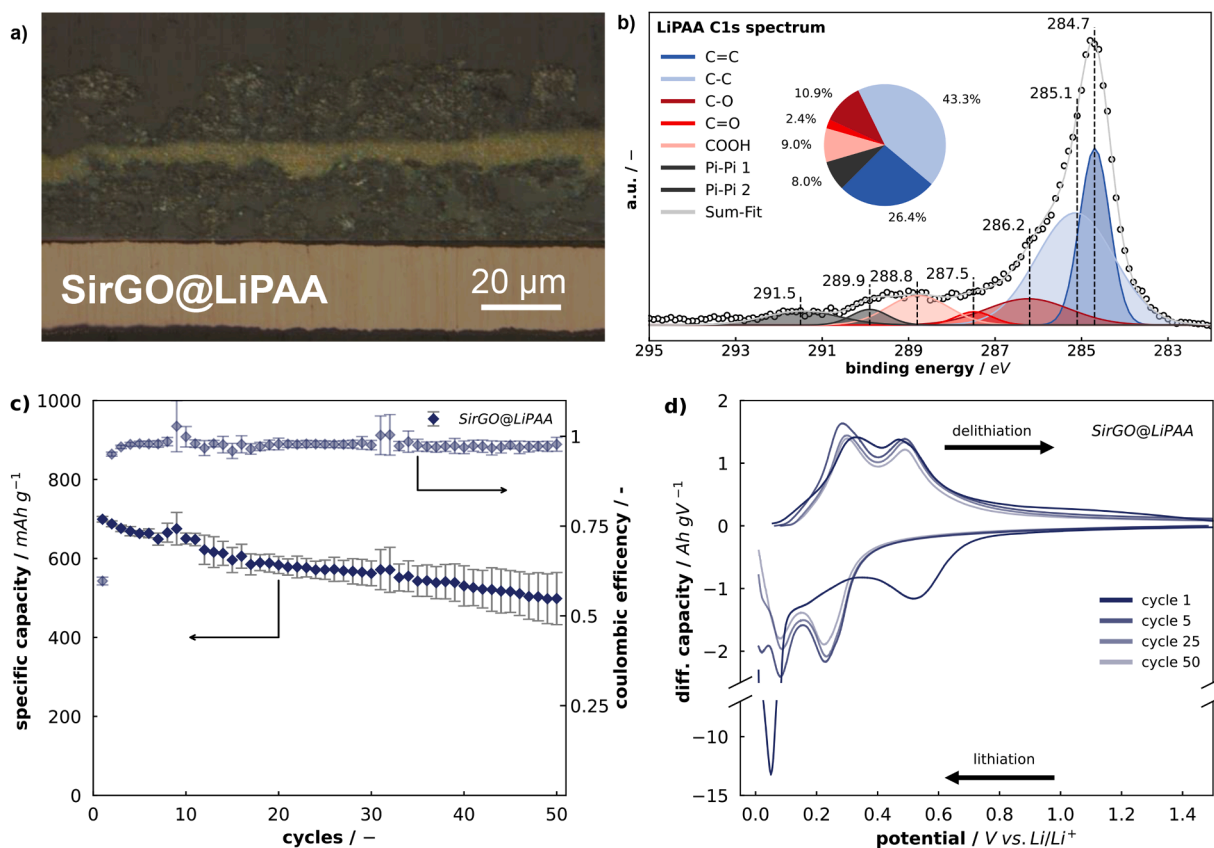
In the prelithiated polyacrylic acid binder Li$^+$-ions partially substitute the hydrogen atoms of the carboxy group. This results in an improved Li$^+$-conductivity of the binder system, which is essential for a sufficiently high cycling performance and reduced lithium consumption during SEI formation [43]. Furthermore, the use of fully prelithiated PAA results in the formation of a more stable and uniform SEI due to the lower viscosity of the ink, resulting in a more homogeneous wetting. Studies conducted by Porcher et al. and Xiong et al. have shown that silicon particles are uniformly coated by a thin layer of the binder when LiPAA was used [33,44]. In contrast, PAA forms a heterogeneous distribution of binder islands deposited on the surface of the silicon particles. Komaba et al. also reached a comparable conclusion regarding graphitic materials [40]. In addition, the polymer chains on the surface of the particles may align more parallel to the surface due to an elongated chain conformation in solution because of the less acidic pH caused by the lithiation of the acrylic acid [44]. This is attributed to the electrostatic repulsion between the charged carboxylate groups. A more coiled conformation can be expected at more acidic pH values, as the chains exhibit intrachain hydrogen bonding in the solution. This different arrangement of the binder on the surface of the silicon and graphite particles affects the mechanical strength of the binder connections at the interparticle junctions, and thus the cohesion of the electrode. Despite the pre-treatment, there are sufficient -COOH groups to ensure proper adhesion of the electrode material on the copper collector which will be discussed further.

A deeper insight into the morphology and the composition of the electrode is provided in Fig. 2.

Fig. 2a shows an optical microscopy cross-section of the spray-coated electrode. Deeper structural insights are given in the SEM cross-sections provided in the Supplementary Information S2–S9. The layer thickness of the electrode material is around 50–60 μm and it shows a uniform silicon interlayer between the rGO layers of approx. 7–8 μm. Due to the manual spraying process, the layer thickness fluctuates slightly. However, a uniform and uninterrupted layer of rGO was successfully deposited onto the silicon layer, resulting in a partial separation of the silicon particles from the electrolyte. Yet, the cross-sectional image also reveals significant porosity within the carbonaceous top layer. On the one hand this can be attributed to the steric structure of the rGO multi-layer graphene [13]. On the other hand, the embedding of electrodes in resin and subsequent polishing results in damage to the surface of the specimen, causing particles to be torn out. This phenomenon leads to an increase in porosity compared to that of the actual electrode, particularly in the upper and exposed electrode layer. The silicon interlayer, which consists of 100–150 nm Si particles, does not show an increased porosity. This particle size as well as the carbonaceous top layer are necessary to prevent Si-particle pulverization and electrical insulation. It can be assumed that contact between the silicon particles and the electrolyte becomes possible due to the porosity of the carbon top layer. Within this interaction volume there is still a risk of unstable SEI formation. To counteract uncontrolled SEI growth, the nm-sized silicon particles were compacted into a uniformly applied μm-thick layer interspersed with binder, which significantly reduces the surface-to-volume-ratio [45,46].

In the following, the C 1s spectrum of the SirGO-electrode spray-coated with LiPAA is discussed in detail. Due to the high surface sensitivity of the characterization technique applied, it can be assumed that the determined types of bonding can be attributed to the binder layer, the interaction with the active materials and the surface of the investigated active materials [47]. This assumption is supported by the FTIR

Fig. 2. (a) Light microscopy cross-section of the SirGO electrode with prelithiated poly acryl acid (LiPAA) and (b) XPS data and analysis of the fitted C 1s excitation. Results of (c) the specific delithiation capacities (vs. Li/Li$^+$) at a current rate of C/10 and (d) the specific differential capacity changes over the investigated potential range in cycle 1, 5, 25, 50 SirGO@LiPAA.

measurements, which have a penetration depth of a few micrometers, provided in the SI, as well as a measurement of the pure powders (Fig. S11) [48]. The carbon-carbon bond ratios in the material vary in comparison to the pure powder. Specifically, for SirGO and SirGO@Li-PAA, the C=C bonds are observed at 284.7 eV with percentages of 28.5 at.% and 26.4 at.% respectively. The C-C bond is found at 285.1 eV $\pm$ 0.1 eV with percentages of 46.4 at.% and 43.3 at.%. The reason for this is the higher proportion of oxygen-containing groups in the binder, specifically C-O at 286.2 eV $\pm$ 0.2 eV, C=O at 287.4 eV $\pm$ 0.1 eV, and COOH at 288.8 eV $\pm$ 0.1 eV. The peak positions are in good agreement with literature [49–51]. Another explanation is the formation of new bonds between the binder and the active component of the electrode during electrode processing. The proportion of oxygen-containing groups in the electrode increases for LiPAA, reaching 22.3 at.% compared to the original 17.3 at.%. In this context, it is important to also consider the type of oxygen-functional groups present. The LiPAA-containing electrode shows an increase in carboxyl groups ratio. These groups interact most strongly with both the functional groups of the rGO sheets and the partially oxidized surface of the nm-Si particles [52,53]. The carboxyl groups that are partially lithiated also interact with the mentioned functional groups, although to a lesser extent [44]. However, these interactions were not considered in this fit. Observing the Si 2p spectra of the analyzed materials (refer to Table 1 and Fig. S10), it is evident that the ratio of pristine to oxidized silicon in SirGO without binder addition is 60 at.% to 40 at.%. After spray-coating, the ratio changes to 35 at.% pristine and 65 at.% oxidized silicon. This shift can be attributed to the spray-coating process itself, during which the nm-Si particles are processed in an aqueous suspension and can thus undergo further oxidation [54,55]. However, the FTIR spectra of the processed electrodes do not show a significant change between 1200 and 1000 cm^{-1} compared to the untreated silicon particles [48]. This suggests that the bulk of the Si particles was not further oxidized. The increase in the Si-O content on the surface of the processed electrodes can also be attributed to the bonds formed between the binder and the silicon particles, indicating good adhesion of the electrodes within the bulk and to the collector foil.

3.1.2. Pull-off adhesion and electrical conductivity measurements

Adhesion pull-off tests were carried out to investigate the mechanical strength of the sprayed layers, their adhesion to each other and to the copper foil. An adhesive strength of 8.7 MPa was found for the SirGO@LiPAA electrode shown in Table 1. The mechanical failure occurs predominantly between the sprayed layers and the copper foil. This indicates strong adhesion within the individual layers and also between the carbon and silicon layer. The first cycle amorphization and the cycle-dependent expansion of silicon, which can reach up to 300% of the rGO-layer's expansion, exposes the electrode to various forces that lead to internal mechanical stresses. Specifically, mechanical stress can occur at the layer boundary between the materials due to the different degrees of expansion. In addition, forces occur within the silicon layer due to its semi reversible volume change (which can be due to pulverization, SEI formation and diffusion limited Li$^+$ trapping). These forces are counteracted by the adhesion of the binder to the particles and the cohesion of the binder between the layers and with respect to the current collector. The XPS data shows a higher content of carboxyl groups in this sample compared to the powder mixture (Table 1, Si/rGO/ACB). This confirms that the adhesion is improved by the higher number of interaction points and interconnects with the particles due to the abundance hydroxyl or carboxylic acid groups present in LiPAA are expected to interact with the surface oxides of Si and rGO [34]. The electrical conductivity of the LiPAA electrode is a result from the superposition of the highly conductive carbonaceous materials and the less conducting silicon. The polymeric binder again lowers the total conductivity. Nevertheless, the use of LiPAA has a positive effect due to the additional conductivity of Li$^+$. Xiong et al. hypothesized that this fact reduces the agglomeration of polyacrylic acid chains due to lower polymer-internal interactions of the hydrogen bonds of carboxyl groups in the suspension.

This should result in a more homogeneous distribution of polymer chains on the partially oxidized silicon particles and a more uniform binder distribution throughout the electrode [44]. This explanation is further supported by our *ex-situ* results of electrode stability and conductivity measurements presented in Table 1.

3.1.3. Electrochemical analysis

To investigate the electrochemical properties of the SirGO@LiPAA electrode, a galvanostatic cycling routine was applied. The results in Fig. 2c show the specific capacity curve of the delithiation over 50 cycles and the corresponding coulombic efficiency. The differential capacity analysis derived from the cycling data is shown in Fig. 2d.

The delithiation capacity is 700 mAh g^{-1} in the first cycle and decreases to 500 mAh g^{-1} after 50 cycles. The standard deviation and with that the initial small variation in degradation increases with increasing number of cycles indicating successively lower reproducibility of the results. A possible reason for this observation is the electrode's inhomogeneity so that different areas degrade at different rates within the up to 7 μm thick Si layer and start to dominate the degradation behavior. The influence of the layer thickness at a constant silicon content is discussed in more detail in the following chapter.

In silicon-containing electrodes, part of the Li$^+$ is irreversibly consumed at the anode, as the coulombic efficiency in Fig. 2c shows. This Li$^+$ loss in nm-sized Si containing anodes can be attributed to the components of SEI formation, pulverization and diffusion limited Li$^+$ trapping [34,56–58]. The first-cycle efficiency is 60 %, which can not only be attributed to this losses. The predominant factor is the irreversible reaction of the remaining functional groups of rGO with the electrolyte, which is consistent with comparable literature and the reference measurements of the pure rGO electrodes (see Fig. 3a and Table 2). A reduction in the total surface area of the electrode has been demonstrated to enhance the ICE and the overall CE but especially in the case of rGO this can also have detrimental effects on the available capacity [59]. In subsequent cycles, the CE increases to a value exceeding 99 %, demonstrating robust behavior over time. The differential capacity analyses shown in Fig. 2d were carried out to obtain more precise information about the processes that occur during cycling. The cycles 1, 5, 25 and 50 are displayed. In the first cycle, the SEI formation and the irreversible reaction of functional groups takes place during lithiation, which is indicated by the broad peak between 0.9 V and 0.4 V. This can be attributed to the decomposition of the used electrolyte, which starts at < 1.0 V [60]. The peak below 0.1 V in the first cycle appears larger as compared to the following cycles. This corresponds to the initial lithiation of crystalline silicon [60]. The silicon is directly and completely lithiated from Li$_0$Si to Li$_{3.75}$Si. The observed progression of the differential capacity curves in the following cycles, however, indicates the uniform growth and formation of the solid electrolyte interphase. This implies that the SEI does not undergo frequent fracturing and breakup due to the cyclic volume change that occurs during the subsequent de/lithiation cycles. Furthermore, renewed decomposition of the electrolyte in a voltage range greater than 0.35 V is not observed and therefore does not occur after its first formation.

The continuous increase in differential capacity starting at 0.4 V in the following cycles can be explained by the lithiation of the reduced graphene oxide comparable to the lithiation of soft carbons as described in the literature [37]. This process shows a maximum at <0.1 V which is superimposed by the lithiation of the silicon phase at 0.25 V, i.e. its conversion from Li$_0$Si to Li$_{2.0}$Si. The complete lithiation of silicon to Li$_{3.75}$Si is indicated by the peak at 0.1 V [61,62]. Looking at the delithiation behavior, a slight shoulder can be observed at around 0.19 V, which can be attributed to the deintercalation of Li$^+$ from rGO [37,60]. The other two peaks at 0.28 V and 0.5 V correspond to the delithiation from Li$_{3.75}$Si to Li$_{2.0}$Si and from Li$_{2.0}$Si to Li$_0$Si [61,62].

From cycle 5 onwards, a decrease in the peak height of the first delithiation peak can be observed. This may indicate that less Li$_{3.75}$Si is converted to Li$_{2.0}$Si. However, when looking at the lithiation behavior it
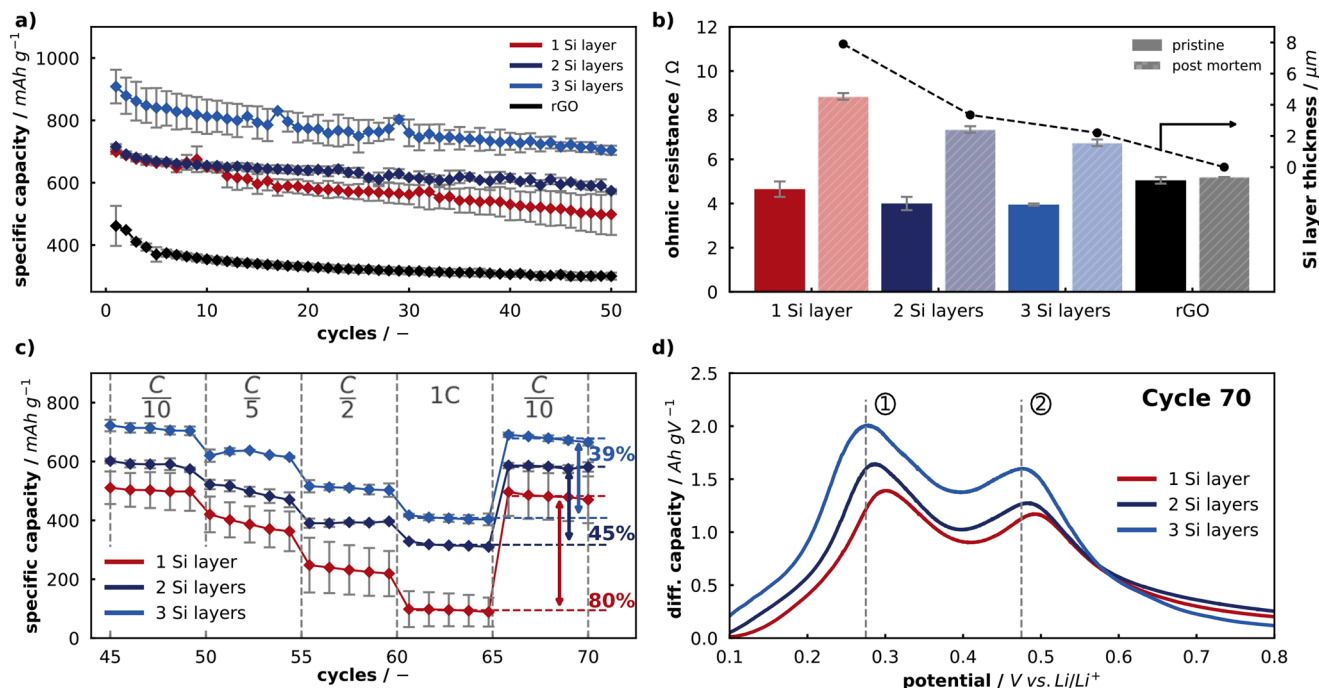
Fig. 3. Results of (a) the specific delithiation capacities of SirGO@LiPAA with 1, 2, and 3 silicon interlayers and pure rGO over 50 cycles at a current rate of C/10 and (b) the ohmic resistance before and after cycling correlated with the single Si layer thickness, (c) C-rate variation, with percentual capacity retention, and (d) the compared differential discharge capacities in the 70ᵗʰ cycle.

Table 2
Summary of electrochemical properties from galvanostatic cycling vs Li/Li$^+$ for rGO SirGO@LiPAA electrodes with 1, 2 and 3 silicon interlayers.

Properties	Unit	rGO	rGO/Si$_{1\ layer}$	rGO/Si$_{2\ layers}$	rGO/Si$_{3\ layers}$
Tot. delit. capacity cycles $_{1-50}$	Ah g^{-1}	16.6 ($\pm$ 3.4 %)	29.0 ($\pm$ 5.6 %)	31.5 ($\pm$ 2.1 %)	38.7 ($\pm$ 4.8 %)
Irreversible capacity 1ˢᵗ cycle	mAh g^{-1}	522.3 ($\pm$ 12.3 %)	472.1 ($\pm$ 1.5 %)	484.2 ($\pm$ 1.7 %)	591.6 ($\pm$ 9.1 %)
Delithiation capacity 1ˢᵗ cycle	mAh g^{-1}	461.48 ($\pm$ 13.9 %)	699.2 ($\pm$ 1.0 %)	715.4 ($\pm$ 1.1 %)	908.5 ($\pm$ 5.9 %)
CE 1ˢᵗ cycle (ICE)	%	46.6 ($\pm$ 8.5 %)	59.7 ($\pm$ 1.7 %)	59.6 ($\pm$ 1.0 %)	60.5 ($\pm$ 1.4 %)
Average CE cycles $_{2-50}$	%	97.8 ($\pm$ 0.5 %)	97.7 ($\pm$ 1.7 %)	98.8 ($\pm$ 0.1 %)	98.1 ($\pm$ 0.1 %)

can also be seen that overall less Li$_{3.75}$Si is formed, and therefore less material will be available for the subsequent delithiation step. As a result of this only incomplete lithiation, the electrode has a lower capacity. The peak hysteresis is less pronounced, leading to the conclusion that LiPAA does not prevent the ageing of silicon, but rather delays it. This may be due to the improved mechanical stability of the electrode and therefore its suppressed delamination from the collector [32,63]. The authors are not aware of any other studies that directly compare the performance of Si/rGO electrodes processed in sandwich structures with LiPAA binders by a spray-coating approach.

3.2. Influence of the number of Si layers

A sandwich-structured composite electrode with one Si interlayer showed a promising approach with this binder system and manufacturing routine. In a next step, the influence of the Si layer thickness as well as the number of alternating silicon layers and with that the electrical and ionic accessibility of the silicon particles were investigated. To address this issue, the number of silicon interlayers was first varied while maintaining a constant silicon content of 17 wt.% in the electrode. The electrodes differed in the number of intermediate silicon layers (one, two, or three), whereby the first layer (on the Cu

collector) and the last layer (electrode surface) were always prepared from rGO.

Fig. 3 illustrates their electrochemical properties in detail. A comparison with literature results is provided in Table ST2 of the SI [26–29]. This comparison indicates that the electrodes produced in this work achieve higher capacities at lower silicon contents while following a significantly simpler fabrication process.

This part of the study emphasizes the effect of the different degradation mechanisms taking place during cycling. With the separation of silicon from the carbon material, local areas of lower electrical conductivity are being created across the electrode layer. With that the slower Li$^+$ diffusion through silicon becomes the dominant rate-limiting process and with that the limiting factor during the de/lithiation [64,65]. To tackle this issue, a minimization of Si layer thickness and concomitant increase in layers would be an obvious solution. However, an increase in the number of layers with a constant silicon content results in a higher surface-to-volume ratio for the silicon particles, and this will again be accompanied by a continuous degradation of the silicon phase.

In Fig. 3a, it can be observed that the electrodes with one and two Si interlayers show comparable capacities in the first cycles. Subsequently, the capacity of the electrodes with one Si layer drops by around 50 mAh

g^{-1} but stabilizes and remains parallel to the capacity of the electrode with two Si layers. Initially, the irreversible capacity is higher for the electrodes with two Si interlayers; however, it decreases to a minimum later during the following cycles. This phenomenon can be attributed to the increased exposed silicon surface resulting from the two layers. The electrode with one Si interlayer exhibits a lower irreversible capacity at the beginning, but the thicker silicon layer leads to faster partial passivation. Therefore, it is hypothesized that during the initial cycles, these two effects occur in a superposition. The electrodes containing three Si interlayers show a higher capacity of approximately 775 mAh g^{-1}, which is still about 25 % higher compared to the capacity of the electrode containing two Si interlayers after 50 cycles. In comparison, the pure rGO electrodes show a significantly lower capacity, which is as expected. The electrodes achieve an efficiency of 46.6 % in the initial cycle, as illustrated in Table 2. Furthermore, a decline in capacity is observed during the initial 10 cycles. This behavior can be attributed to the high specific surface area (179 $m^2 g^{-1}$, Table 1) and the high number of functional groups. The high capacity as well as the high capacity loss observed in the initial cycles of rGO can be attributed to reactions of a semi-reversible nature. These reactions involve semi-reversible de-/lithiation mechanisms with the remaining oxygen and hydrogen-containing functional groups in the carbon lattice. Additionally, the decomposition of the electrolyte at the defect sites of thermally reduced rGO must be considered [37]. An inverse effect can be observed in the scattering of the results. The standard deviation of the electrodes with three silicon interlayers gets smaller as the number of cycles increases, whereas that of the electrodes with a single Si interlayer increases. We assume that the observed behavior is due to two opposing degradation processes. An increase in the number of layers, and thus the contact surface between silicon and electrolyte, initially results in greater fluctuations in the reversible capacity. However, this situation stabilizes as the passivation layer is fully formed over the course of the cycles. In contrast, the single layer exhibits the opposite behavior. As the number of cycles increases, electrodes from the same batch display increasingly disparate behavior due to the inactivation of arbitrary parts of the electrode by pulverization.

Fig. 3b shows the ohmic resistance with increasing number of Si interlayers and with that a decrease in the individual layer thickness in comparison to a pure rGO electrode. The cell resistances of the electrodes were determined by analyzing impedance spectra before cycling (pristine) and after 50 cycles with a constant C-rate of 1/10 as well as a variable C-rate of 1/5, 1/2, 1, and again 1/10 for 5 cycles each (post-mortem). No significant increase in ohmic resistance was observed in the cells before cycling. The uniform ohmic resistance before cycling may be explained by the fact that the proportion of the ohmic resistance attributed to the differently designed silicon interlayers plays only a minor role compared to the ratio of conductivity associated with the electrolyte, the binder and the rGO layers [66]. In addition, no SEI has yet been formed here and ageing effects due to delamination or continuous growth of the passivation layer are not yet significant. The post-mortem samples exhibit a more pronounced trend in comparison to the pristine samples before cycling. In general, they demonstrate a higher ohmic resistance due to SEI formation, whereas the formation of the passivation layer on the rGO intermediate layers does not appear to be significant when comparing the results before and after cycling for the pure rGO electrode. Another reason for the increased resistance may be the degradation originating from the continuous SEI growth on the nm-silicon particles and the delamination of the whole layer [7,67].

The results in Table 2 indicate that the loss of active material in the 1st cycle due to SEI formation is directly proportional to the accessible free silicon surface and thus to the number of layers. The proportion of silicon that becomes inaccessible after the initial lithiation (ICE) is directly related to the thickness of the silicon layer and the associated lithium trapping. The irreversible capacity is therefore the highest for electrodes with three intermediate Si-layers, as shown in Table 2. However, the results from Fig. 3a and the coulombic efficiencies of the

initial cycles demonstrate that the effect of lithium trapping is the predominant cause of the reduced capacity of the electrodes with thicker silicon interlayers. This is in good agreement with the SEM/EDS analysis and the GITT measurements shown in Figs. 6g–j, S2–9 and 5a and b. Therefore, it appears that increasing the silicon surface area exposed to the electrolyte directly results in a more pronounced SEI formation on the particles causing a capacity decrease in the first cycle, which stays stable within the subsequent cycles. This is partly due to the higher flexibility and mechanical stability of the LiPAA binder described before [68]. If, on the other hand, the thickness of the Si layers decreases, the opposite effect occurs and the ohmic cell resistance decreases, as shown in Fig. 3b. This indicates that the passivation layer has less influence on the ohmic cell resistance of layered electrodes compared to fully intermixed nm-Si/C electrodes with a high surface-to-volume-ratio of the silicon particles [46]. The performance of the electrodes benefits from the enhanced electrical and ionic accessibility of individual silicon particles within the thinner layers. Nevertheless, the potential impact of an alternating thin-layer strategy with a number of layers ≥ 4 on the electrochemical and mechanical properties remains to be confirmed. This would also result in experimental limitations, as spray-coated layers have a limited minimum thickness and electrodes have a maximum thickness for optimal performance.

This clear trend can also be observed for the C-rate variation shown in Fig. 3c. The electrodes were analyzed over 5 cycles at increasing currents. Due to diffusion limitations and the rising cell resistance, the specific capacities decrease as the current increases. It is evident that the specific capacities of the different electrodes continue to diverge as the current gradually increases. The decrease in current back to 1/10 C resulted in an increase in capacity. This indicates that all the electrodes analyzed were able to withstand the higher C-rates without pronounced degradation. Thinner Si layers exhibit higher fast-charging capacity. For instance, increasing the charging current from 1/10 C to 1 C reduces the capacity for the 7.1 μm thick Si layer by 80 %. In contrast, electrodes with a Si layer thickness of 3.4 μm and 2.2 μm show a reduction in capacity of only 45 % and 39 %, respectively. This suggests an increase in charge exchange without stronger passivation of the electrode due to a higher number of silicon surfaces exposed to the electrolyte. For a more detailed insight, the voltage-resolved capacities at the different C-rates are given in Fig. S12.

Our hypothesis to explain the behavior during both constant cycling and C-rate variation is summarized in Fig. 3d. Here the voltage-resolved specific capacity change during delithiation in the 70th cycle is shown. This cycle was chosen because the degradation of the electrodes is most advanced and is therefore most clearly visible here. Depending on the thickness of the silicon layer, the through-plane conductivity of the pristine electrodes changes only slightly (see Fig. 3b). However, the electrochemical accessibility of the Si particles in the layer becomes more challenging with thicker individual layers due to the increased path length through a region of lower conductivity. Furthermore, the effect is intensified by the expansion in volume of this layer during the cycling process, as illustrated in Figs. S2–S9. Fig. 3d shows the voltage-resolved specific capacity changes of the three investigated types of electrodes with a shift of the delithiation potential ((1) $Li_{3.75}Si \rightarrow Li_{2.0}Si$ and (2) $Li_{2.0}Si \rightarrow a\text{-}Si$). This shift increases with increasing Si layer thickness at a constant Si content of 17 wt.%. At higher C-rates, these electrodes have a lower specific capacity, because some areas are no longer electrochemically accessible due to the shift of the de/lithiation voltage to areas outside the operating window (see SI Fig. S12a–f) also based on an increased pathlength through a region of lower electrical conductivity. It is also noticeable that the three electrodes do not have the same specific capacity, despite having the same amount of theoretically accessible silicon. We propose that a thicker Si layer does not only result in a hysteresis with respect to the de/lithiation potentials, but also affects the maximum electrochemically available fraction of silicon from cycle 1 onwards. A more detailed analysis is given in Figs. S12 and S13 in the supplementary information. During the formation (cycle 1), the

differential capacity changes differ in terms of the position of the maxima from subsequent cycles due to the initial lithiation of the crystalline Si nanoparticles (<0.1 V vs. Li/Li$^+$) and the formation of the solid electrolyte interphase (1–0.4 V vs. Li/Li$^+$). Fig. S13b and c illustrate the intensity reductions, shifts in the de/lithiation potentials, and resulting increasing hysteresis for cycles 5 and 70. The results indicate that a thinner, but higher number of Si layers is more advantageous for maximizing the electrode's capacity. However, this result is achieved at the cost of a higher continuous capacity fade due to the increase in Si surface area, which does not appear to be critical in this study. The next section will highlight analyses of SirGO electrodes with critical layer thicknesses to support our hypothesis.

3.3. Discussing the effects of Si content and Si layer thickness

To investigate the influence of the Si content and thus the increased pathlength through a region of lower electrical conductivity and its influence on the electrochemical accessibility of the Si particles, electrodes with 3 Si-interlayers each were produced. The Si content of the different composite electrodes varied between 17, 26, and 39 wt.%. The variation of the Si content has a direct effect on the layer thickness, which increases with increasing Si content (see table ST1). In Fig. 5, the electrochemical properties of the composite electrodes are first examined in more detail and compared with each other. To visualize the impact of degradation on the potential-dependent capacity and its influence on capacity fade, the following figures present the cycling data of an exemplary cell for each silicon content, further results are shown in Fig. S17. It should be noted here that we did not average values, including standard deviations, as this would result in cancellation effects.

Fig. 4a shows the delithiation capacity curve of the composite electrodes with different Si contents over 50 cycles. The electrode with 14 wt.% Si initially has the highest capacity with 962 mAh g^{-1}. The lowest delithiation capacity with 820 mAh g^{-1} in the first cycle is shown by the electrode with 26 wt.% Si. Both electrodes demonstrated stable capacity retention over the cycles, with only minor capacity fluctuations. Nevertheless, the capacity of this electrode exhibits a slightly

greater decrease over the 50 cycles than the 26 wt.% Si electrode. The enhanced silicon surface leads to more SEI being formed, which in turn accelerates the degradation of the electrode. The electrode with 39 wt.% Si has an initial capacity of 904 mAh g^{-1}, which decreases from the 5th cycle onwards. Martín-Yerga et al. attribute this behavior to the continuous SEI formation [69]. This is followed by strong capacity fluctuations that follow a repetitive pattern. Their origin is shown in more detail in Figs 6 and 7.

Fig. 4b illustrates the impact of higher silicon content on the capacity retention at increased C-rates. The observed trend that higher silicon content has a negative effect on capacity is also evident here. The capacity loss of the electrode with 14 wt.% Si between the 1 C and 1/10 C-rate is 42 %, whereas it is 94 % for the electrode with 39 wt.% Si. Again, reduced accessibility due to thicker silicon layers can be held responsible for this behavior. In addition to the low capacity, this also results in poor fast charging capability.

The change in Li$^+$ diffusivity during the de-/ lithiation processes is illustrated in Fig. 5 and indeed corroborates the assumed effect.

Fig. 5a and b display the Li$^+$ diffusion coefficients of the investigated electrodes. To ensure comparability with the data presented in Fig. 4, the corresponding GITT analyses were performed with a C-rate of 1/10 C. The electrochemical diffusion kinetics were examined using the following simplified equation published by Weppner and Huggins:

$$D_{Li^+} = \left(\frac{4l^2}{\pi \Delta t_p}\right)\left(\frac{\Delta E_s}{\Delta E_t}\right)^2 \tag{1}$$

In this context, l is defined as the characteristic diffusion length, while Δt_p represents the time of the constant current pulse. The term ΔE_s is used to quantify the difference in the open circuit potential at the end of two consecutive open circuit relaxation periods, ΔE_t represents the potential change that occurs when the test current is applied, which is corrected by the ohmic potential drop. The equation is valid within very small time domains $t \ll \tau$. In this case, τ represents the diffusion time constant, which is equal to l^2/D. This ensures an accurate approximation of the Fick's diffusion principles [70,71]. The calculated results are in good agreement with those reported in the literature on Si/C-composite
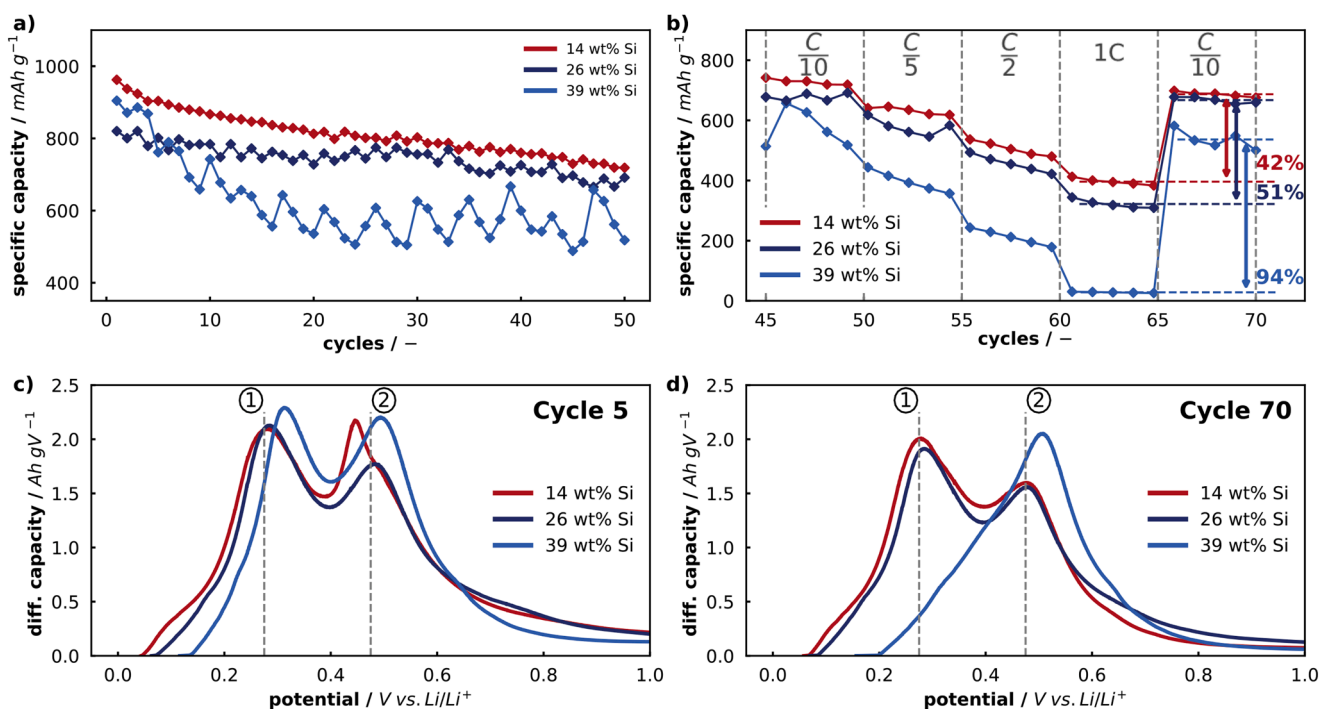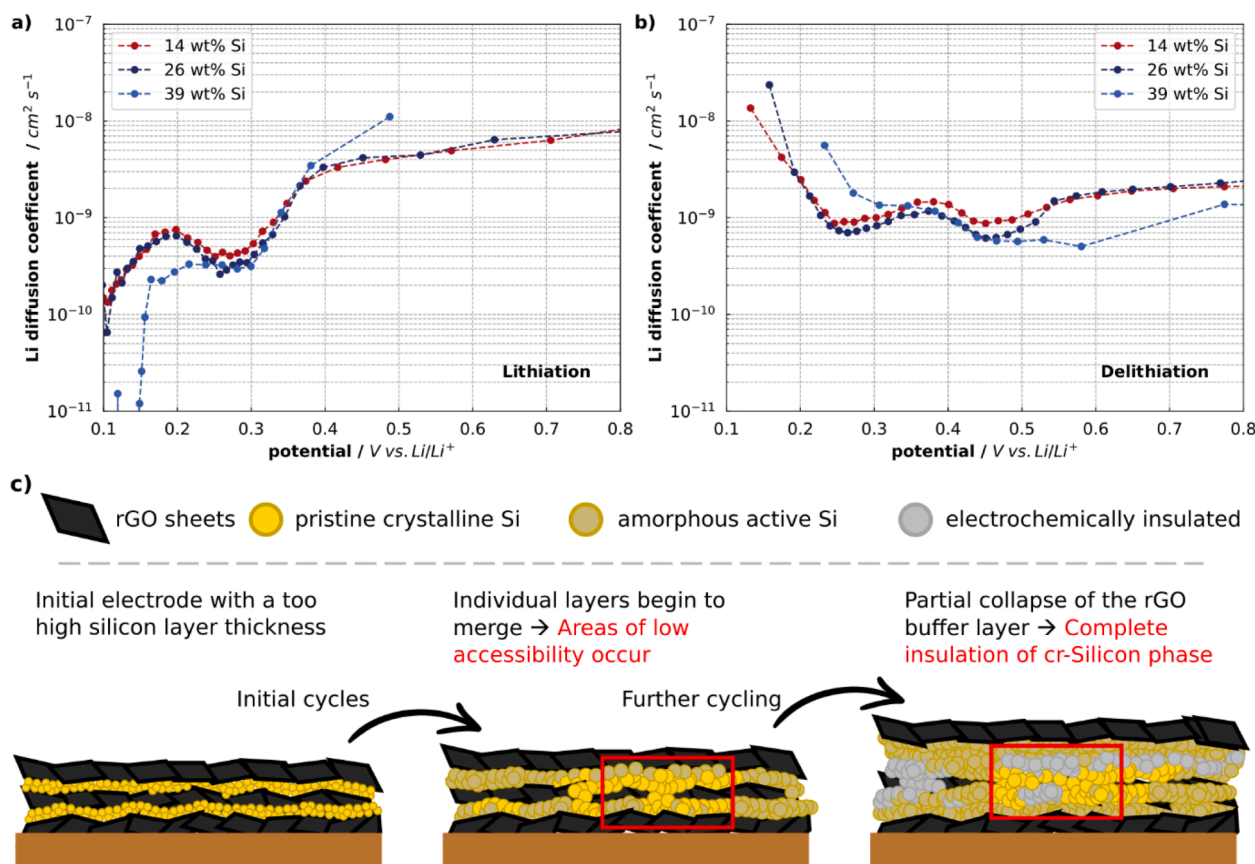

Fig. 4. Results of (a) the specific delithiation capacities SirGO@LiPAA with 14 wt.%, 26 wt.% and 39 wt.% silicon with 3 Si-interlayers vs. Li/Li$^+$ over 50 cycles at a current rate of 1/10 C and (b) C-rate variation, with percentual capacity retention, (c) and (d) the compared differential charge capacities in the 5th and 70th cycle.

Fig. 5. Li$^+$ diffusion coefficients resulting from the GITT measurements for the investigated electrodes with 14 wt.%, 26 wt.% and 39 wt.% silicon with 3 Si-interlayers vs. Li/Li$^+$ during the (a) lithiation and (b) delithiation process. (c) Schematic illustration of the degradation phenomena causing the electrochemical isolation of uncycled silicon fractions.

materials, which also range between 10^{-8} – 10^{-11} cm^2 s^{-1} [29,70,72] and are with that between pure silicon electrodes which range between 10^{-12} – 10^{-14} cm^2 s^{-1} [64,73] and different carbon electrodes ranging between 10^{-6} – 10^{-9} cm^2 s^{-1} [74,75].

The diffusion coefficients presented were recorded after five cycles in order to eliminate the potential effects of electrode ageing and degradation influencing the Li$^+$ diffusion. It can be observed already at this early stage, that the two electrodes with 14 and 26 wt.% of silicon exhibit a stable diffusion coefficient curve, whereas the electrode with 39 wt.% displays significantly lower diffusion coefficients. During lithiation, a minimum can be observed at a voltage of 0.28 V vs Li/Li$^+$, which corresponds to the lithiation voltage of amorphous silicon [2,61,62]. At this lithiation voltage, the 39 wt.% electrode exhibits a comparable diffusion coefficient of approximately 9×10^{-9} cm^2 s^{-1}. However, this value is significantly lower, resulting in a difference of more than one order in magnitude at the lithiation voltage of 0.1 V, indicating an unsatisfying lithiation behavior. Taking Fig. 5b into account, this hypothesis can be confirmed. The electrodes with 14 wt.% and 26 wt.% show diffusion coefficients of 2×10^{-9} cm^2 s^{-1} and 4×10^{-9} cm^2 s^{-1} in the same order of magnitude and at the same delithiation potentials (0.28 V and 0.47 V). These observations are also reflected in the differential capacity analyses shown in Fig. 4c. In the case of the electrode with 39 wt.%, a shift in the delithiation minima can be determined, with only one minimum at 0.5 V to 0.6 V. The diffusion coefficient is also approximately 10^{-9} cm^2 s^{-1}.

Considering Fig. 4c the potential shift observed in the electrode with 39 wt.% Si indicates a change in the delithiation behavior, where peak 1 increases from 0.28 V to 0.32 V, corresponding to the Li$_{3.75}$Si → Li$_{2.0}$Si process, and peak 2 shifts from 0.48 V to 0.5 V, representing Li$_{2.0}$Si → a-Si transition. These shifts, in conjunction with

changes in the Li$^+$ diffusion coefficient, suggest that a silicon content of 39 wt.% strongly disrupts the lithiation/delithiation kinetics, likely due to alterations in the electrode's electrochemical properties. Upon examination of Fig. 4d, it becomes evident that after the following 70 cycles, the initial peak at 0.315 V becomes insignificant and only appears as a negligible shoulder, while the subsequent peak at 0.5 V remains distinctly pronounced.

Considering the results of Figs. 4 and 5, it can be concluded that there is another degradation mechanism in addition to those already discussed in the context of Fig. 3 and Table 2. This further degradation mechanism is attributed to the influence of an expanding silicon interlayer on another Si-layer resulting from the expansion beyond the rGO interlayer, the silicon to carbon layer thickness ratio. This secondary effect is illustrated schematically in Fig. 5c. This effect occurs as soon as the silicon layers can influence each other, since only then areas occur where the rGO loses its supporting function, which is intended to partially buffer the silicon expansion and thus prevents pulverization of the electrode structure [76]. As the quantity of silicon per layer and, consequently, the thickness of the individual silicon layer increases, the ratio of rGO to Si between the layers also declines. As the individual Si layers expand (pristine > 4 µm) due to ongoing SEI formation, the rGO buffer layer is unable to maintain its integrity. This results in the merging of the Si layers and the displacement of the rGO, as evidenced by the SEM-EDS images shown in Fig. 6i, j and S2–S9. The electrodes were compared pristine and post-mortem in the discharged state. The expansion is therefore not attributable to the lithiated state of the still intact areas of the electrode. The expansion of the electrode is due to SEI formation, the Li$^+$ trapping and the amorphization of the silicon interlayers. This phenomenon can be regarded as a self-reinforcing effect, i.e. getting more pronounced with time, as it creates larger areas of low
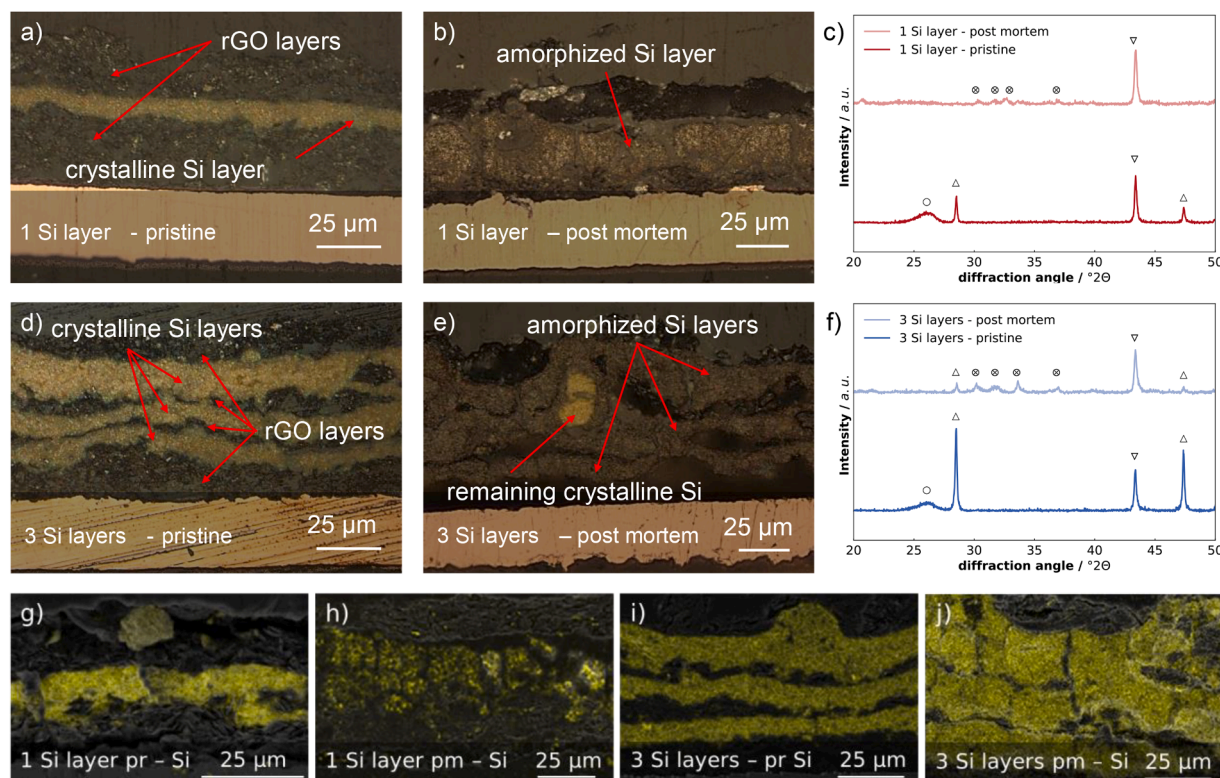
Fig. 6. Light microscopy cross-sections of a 1 Si layer 14 wt.% silicon electrode (a) before and (b) after cycling, a 3 Si layer 39 wt.% silicon electrode (d) before and (e) after cycling, XRD patterns of the (c) 1 Si layer electrode in both states as well as the pattern of the (f) 3 Si layer electrode. In c) and f) the symbols correspond to the following lattice planes at 2θ: ○= (002) reduced graphene oxide at 25.4 ° [13,79,80], △= (111) silicon at 28 ° and (220) silicon at 46.9 ° [81,82], ▽ = (111) copper at 43 ° [83]], ⊗ =, = (111) lithium carbonate at 29.5 °, (202) lithium carbonate at 31.3 °, (002) lithium carbonate at 32.2 ° and (31-1) lithium carbonate at 37.2 ° [84,85] and SEM/EDS-measurements of the Si signal for the 1 Si layer electrode (g) before, (h) after cycling as well as for the 3 Si layer electrode (i) before, (j) after cycling.

conductivity that are suddenly no longer electrochemically accessible, see illustrated in Fig. 5c. As illustrated in Fig. S14c, a complete lithiation of the Li$_{3.75}$Si phase does not occur during the lithiation of the 70th cycle for the electrode with 39 wt.% silicon. The lower specific capacity compared to the other electrodes has been concluded from the weak and barely perceptible peak at 0.315 V.

The incomplete electrode lithiation is due to hysteresis of the second lithiation step (Li$_{2.0}$Si → Li$_{3.75}$Si) towards voltages < 0.01 V, as lower voltages are outside the cycling window. This shift is caused by the increased internal cell resistance due to SEI formation, and locally higher ohmic resistances due to the electrical insulation of parts of the active material [77]. The remaining resistances can be attributed to the electrode components that are kept electrochemically accessible, analogous to a locally higher C-rate [78].

In Fig. 6 light microscopy cross-sections of the two electrodes with the highest irreversible capacities are compared in terms of morphology and crystal structure to point out possible causes of this capacity loss before cycling and post-mortem.

Due to the different visible light absorption behavior and the resulting different colors, silicon and carbon can be easily distinguished from each other. In this instance, the crystalline, pristine silicon appears golden, while the carbon matrix appears black. Post-mortem examinations also allow a separation between the two materials. Due to the intercalation processes during cycling, silicon is no longer crystalline but amorphous [2,62], which makes it appear darker under the light microscope than in the crystalline state. Nevertheless, the difference to rGO is easily recognizable. The electrode with a single silicon interlayer, Fig. 6a, exhibits a Si-layer thickness of 7 µm before cycling. Afterwards the silicon layer appears completely amorphous and has an increased thickness by a factor of 2 to 3, shown in Fig. 6b. The XRD pattern of the

pristine electrode, as depicted in Fig. 6c, exhibits a broad reflection that can be attributed to reduced graphene oxide, with a peak position at 25.4 °. The reflex for copper at 43 °, which is due to the signal of the current collector, ensures complete penetration of the XRD signal through the entire electrode. The two reflections at 28 ° and 46.9 ° can be assigned to crystalline silicon. The diffractogram of the pristine electrode with three silicon interlayers shows identical reflexes, with the only difference that the height of the silicon reflexes are dominant due to the higher silicon content. In the electrode with one silicon layer, the post-mortem light microscopy cross-sections show only amorphous silicon. The XRD measurement also confirms that no crystalline silicon portion remains in the electrode, due to the missing reflexes at 28 ° and 46.9 °. The small reflexes at 29.5 °, 31.3 °, 32.2 ° and at 37.2 ° indicate lithium carbonates, which are formed during SEI growth [84,86]. A stronger signal in the diffractogram of the electrode with three silicon layers indicates a higher SEI content, which is attributed to a higher total silicon content and consequently a larger silicon surface area exposed to the electrolyte. In addition, the thickness of the individual silicon layer of 8 µm for the electrode with three interlayers (Fig. 6d) is only slightly higher compared to the electrode with only one Si interlayer (Fig. 6a).

The post-mortem light microscopy cross-section of the electrode with 39 wt.% shown in Fig. 6e indicates that crystalline silicon areas remain within the amorphous silicon layers, comparable to the schematic illustration in Fig. 5c. This is confirmed by the post-mortem XRD measurements, which also show reflexes at 28 ° and 46.9 °. The hypothesis for this kind of degradation is a different degree of expansion of individual areas within the silicon layer due to ununiform de-/lithiation of the electrode [87], which requires a subdivision of the different conditions of silicon:

- amorphized silicon areas near the rGO interlayer which de-/lithiate completely and thus undergo a volume change of up to 300%,
- amorphized silicon areas that are further inside the silicon layer and can only be partially de-/lithiated due to the diffusion-limited Li$^+$ trapping [57,88] and thus undergo a smaller volume change,
- amorphized silicon areas that are even deeper within the silicon layer and are no longer electrochemically accessible [58], resulting in no further volume change and
- crystalline silicon areas that have not yet undergone any volume change [87].

Due to the varying expansion of the distinct layer components, a layer fracture will occur as the interface structure between the silicon and carbon layers undergoes modifications. Due to mechanical stress the cohesion between the layers is exceeded if the silicon expansion is too high and the buffering rGO-layer is displaced. Saidi et al. have demonstrated through simulation that the process of lithiation induces a complex local stress field, which influences the structural, physical, and chemical properties of pure silicon electrodes [89]. This phenomenon is primarily attributed to the amorphization of crystalline silicon, resulting in the induction of high local pressures. This study, in conjunction with other research groups, further conclude that pressure-absorbing structures can prevent the occurrence of excessive mechanical stresses [89, 90]. This finding aligns with our hypothesis that the failure of the rGO buffer layer contributes to the enhanced degradation observed. The formation of zones of different (de)lithiability within Si/C electrodes and their influence on the electrochemical and mechanical stability can also be confirmed experimentally [87,91,92]. Furthermore, a Li$^+$-gradient accumulates towards the center of the particles [87] or in our case layers. This results in lithium trapping and a consequent, substantial increase in irreversible expansion within the electrodes [91,92].

Consequently, areas that were already inactive can be made accessible again or silicon particles in pristine condition can be exposed anew, which in turn leads to increased SEI formation. This, in turn, results in an increased SEI formation, a further growth of the layer, and a decrease in capacity that fluctuates over time.

This conclusion can be derived from the comparison of pristine and post-mortem SEM-EDX images of the different electrodes (SI S2–S9), as well as remaining crystalline areas in Fig. 6 e, f. To validate this theory, additional measurements were performed with a 20 h CV step during formation (SI Fig. S17). Here periodic fluctuations still appear; however, these fluctuations were significantly diminished. This phenomenon can be attributed to the fact that there is no pristine silicon surface exposed to the electrolyte, resulting in less electrolyte decomposition. Fig. 7a–c provides a more detailed explanation of how this effect influences the electrochemical performance. It represents the voltage-resolved differential capacity analysis of the electrodes with 39 wt.%, 26 wt.% and 14 wt.% silicon, each with three silicon interlayers, in the range between cycle 29 to 33. This representation has been chosen to demonstrate the electrochemical activation and deactivation of initially inaccessible crystalline silicon fractions. To show the influence of this repetitive (de-) activation processes, the change of the voltage resolved delithiation capacity over 50 cycles has been depicted in the form of heatmaps of the 3 electrodes investigated and compared in Fig. 7d-f.

From Fig. 7a to c, it can be easily seen that fluctuation in capacity decreases. Furthermore, the differential capacity analysis of the cycles 29 to 33, shown in Fig. 7a to c, indicates that the peak heights representing the stored capacity stabilize with decreasing silicon content. The electrode with 39 wt.% silicon exhibits pronounced, periodic fluctuations in capacity retention occurring at approximately every 4-5 cycles. The 29th cycle initially represents a local minimum in the capacity curve. The voltage-resolved differential capacity curve in Fig. 7a shows a peak
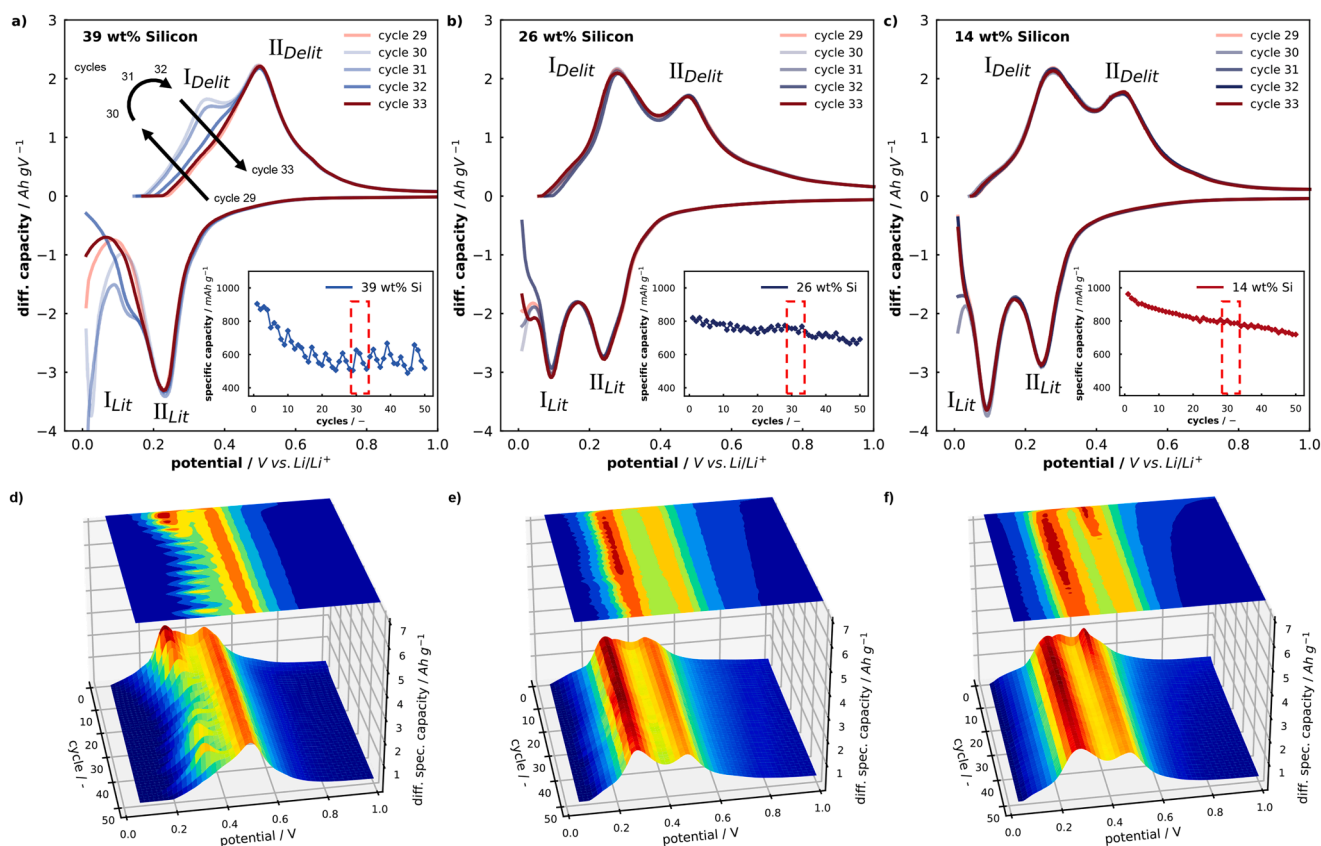
Fig. 7. Differential capacity analysis of an electrode with (a) 39 wt.% silicon, (b) 26 wt.% silicon and (c) 14 wt.% silicon and three silicon interlayers in the range from cycle 29 to cycle 33. Followed by a 2 and 3 dimensional heatmap of the differential specific delithiation capacity vs. the potential over 50 cycles for the corresponding electrodes with (d) 39 wt.%, (e) 26 wt.% and (f) 14 wt.% silicon.

at 0.23 V vs Li/Li$^+$ for that cycle corresponding to the lithiation of the amorphous silicon phase up to a state of Li$_{2.0}$Si (II$_{lit}$). The associated delithiation shows a maximum at 0.5 V vs Li/Li$^+$ (II$_{delit}$), which indicates that only lithiation into the Li$_{2.0}$Si phase has taken place. For this reason, the delithiation capacity is reduced.

The impact of the observed effect decreases with decreasing amount of silicon in the electrode and therefore with thinner silicon interlayers. This results in a quasi-stable de-/lithiation behavior for the electrode with 14 wt.% silicon shown in Fig. 7c. The peak positions at I$_{Delit}$ at 0.275 V vs Li/Li$^+$ (Li$_{3.75}$Si → Li$_{2.0}$Si) and at II$_{Delit}$ at 0.475 V vs Li/Li$^+$ (Li$_{2.0}$Si → a-Si) do not change during the observed delithiation cycles. Slight variations are, however, observed in the region of the lower termination criteria between 0.05 to 0.01 V vs Li/Li$^+$ in the 32nd and the 33rd cycle during lithiation. This is consistent with a slight capacity fade during delithiation in cycle 32 and a following increase in cycle 33. Nevertheless, the lithiation potentials for I$_{Lit}$ at 0.1 V vs Li/Li$^+$ and II$_{Lit}$ at 0.24 V vs Li/Li$^+$ remain unchanged, indicating a stable cycling behavior of the cell with complete lithiation up to the fully- lithiated state Li$_{3.75}$Si of the already amorphous silicon phase [61,62].

A comparison of the initial ohmic (Fig. S15a) and charge-transfer resistances (Fig. S15b) of the electrodes reveals that they are almost identical before cycling. The ohmic resistances of the 26 wt.% and 39 wt. % electrodes are slightly higher, resulting in slightly increased voltage hysteresis. The impact of partial lithiation of electrodes with a higher silicon content cannot be attributed solely to voltage hysteresis. Upon examination of the initial cycles after formation (Fig. S16), it can be observed that all electrodes exhibit identical lithiation behavior, regardless of the silicon content.

Looking at the electron charge transfer resistance (Fig. S15b), it can be noted that the pristine values are similar. There is no clear trend as a function of silicon thickness or silicon content. However, after cycling a tendency of R$_{ct\ 14wt.\%}$ > R$_{ct\ 26wt.\%}$ > R$_{ct\ 39wt.\%}$ becomes apparent. This indicates an increasing passivation of the silicon phase in the electrode due to electrochemical isolation of individual silicon clusters. The charge transfer resistance of the whole electrode decreases with increasing silicon content, as the components with slower reaction kinetics, in this case silicon, become increasingly isolated. In the case of the electrode with 14 wt.% silicon, a large proportion of the silicon component remains electrochemically active. This results in a higher R$_{ct}$, which is composed of the more conductive carbon and the less conductive silicon components of the electrode. This effect is further enhanced by the fact that the resistance of the remaining electrochemically accessible silicon particles is increased by the SEI formed. If the degree of utilization of the active material of the electrode ($\zeta_c = c_{delit} / c_{delit\ theo.}$) is considered, a trend of $\zeta_{c14wt.\%}$ > $\zeta_{c26wt.\%}$ > $\zeta_{c39wt.\%}$ is obtained. This supports the hypothesis that with increasing silicon content, and hence interlayer thickness, less and less silicon gets lithiated even in these highly porous electrodes. Although the electrode with 26 wt.% silicon still exhibits the same charge/discharge profile (I and II are de-/lithiated), the formation of excessively thick silicon layers and the resulting lower Li$^+$ diffusivity seem to impede the complete de/lithiation of the potentially available active material.

An enhancement in capacity is observed in cycle 30 for the electrode with 39 wt.% silicon. In contrast to cycle 29, this cycle exhibits a peak during the lithiation process at voltages 0.1 V vs Li/Li$^+$. The voltage profiles of the formation cycles of the results presented here (Fig. S14a) again indicate the lithiation of crystalline silicon to the lithium rich Li$_{3.75}$Si phase in good agreement with [60].

The lithiation of pristine crystalline silicon enables the delithiation of this phase (I$_{Delit}$), thereby achieving higher capacities. The delithiation potential of this newly accessible active material is electrochemically indistinguishable from the delithiation potential of the already activated, amorphous silicon at 0.275 V vs Li/Li$^+$ (Li$_{3.75}$Si → Li$_{2.0}$Si). The new accessibility of crystalline silicon may have been facilitated by a break-up or delamination of the SEI [93].

In the 31st cycle, an increase in capacity can be identified during lithiation at 0.12 V vs Li/Li$^+$ next to the II$_{Lit}$ peak at 0.23 V vs Li/Li$^+$, which can be attributed to the lithiation of the Li$_{2.0}$Si to the Li$_{3.75}$Si phase. The fact that this shoulder appears immediately after the activation of previously crystalline silicon suggests that this increase in capacity is related to the freshly exposed silicon active material. During the delithiation process, the I$_{Delit}$ peak at 0.275 V vs Li/Li$^+$ is also present, although to a lesser extent than in the 30th cycle, which is expressed in a slight decrease in capacity.

Subsequently, in the 32nd and 33rd cycle there is a significant decrease in capacity, as evidenced by a reduction of the I$_{lit}$ und I$_{delit}$ peaks. Lithiation and delithiation primarily occur in the Li$_{2.0}$Si phase, indicating that the theoretical capacity of silicon cannot be fully utilized. This phenomenon can be attributed to the excessive growth of the SEI and the electrochemical deactivation due to a growing diffusion limitation. The presence of crystalline silicon areas in the cross-section after cycling indicates that this process continues until these areas are utilized or can no longer be electrochemically accessed due to an excessively thick SEI.

We postulate that this phenomenon is the result of the complex interplay between several factors. When the electrode with a single Si interlayer (Figs. 3 & 6a–c) is considered, it can be observed that an increase in the layer thickness invariably leads to a reduction in the degree of utilization that is already evident in the first cycle. This can be explained by the fact that an electron and a lithium-ion gradient forms in the thicker Si interlayer, due to the SEI formation, the lower local ion and electron concentration, a higher charge transfer resistance and lower Li$^+$ diffusivity (Figs. 5 and S2–9). The resulting local potential is insufficient to initiate the dealloying reaction. As a result, the silicon portion of the layer can be fully lithiated initially, but parts of it passivate after the first charge cycle and cannot be delithiated. A comparison of the lithiation capacity of electrodes with several silicon interlayers and a silicon content of 26 or 39 wt.% (Figs. 4 & 7) reveals that electrodes with a higher silicon content do not deliver the expected higher specific capacities. Firstly, the higher Si content in the 39 wt.% electrode is responsible for the decrease of the through-plane conductivity of the electrode and also a lower ion mobility. This results in a hysteresis of the lithiation potentials, but is not responsible for the capacity fluctuation, as this effect does not occur in the electrode with the same layer thickness and only one intermediate layer.

The incomplete lithiation of the electrode material which causes the fluctuation already during the initial cycles is attributed to two factors: The decreased electrical conductivity resulting from the higher silicon (Si) content of the overall electrode and the increased path length within the individual Si layers. This interplay between diminished electrical conductivity and limited lithiation depth highlights the necessity for an optimized electrode architecture. To effectively address these challenges a promising solution is the presented approach of employing electrodes with an alternating layer structure. For achieving high silicon contents, the utilization of multiple thinner interlayers is recommended, as the higher irreversible capacity during the formation process is not the limiting factor. This is further supported by the results presented in Table 2. The potential effect of an alternating thin-layer approach with four or more layers on the electrochemical and mechanical properties has yet to be verified.

4. Conclusions

In this study, alternatingly structured multilayer anodes of reduced graphene oxide and silicon with different compositions have been successfully fabricated using a spray-coating process. Due to the chosen manufacturing approach, an increased binder content of up to 25 wt.% is required to ensure both satisfactory adhesion to the copper substrate and sufficient cohesive bonding within and between the layers. The choice of a suitable binder system therefore has a significant impact on the performance of the electrode. Prelithiated polyacrylic acid was found to be a suitable water-based system compared to systems with more harmful

solvents such as NMP.

Moreover, the top-down approach adopted here provides an extremely cost-effective and easily scalable method for the controlled deposition of individual layers and leads to enhanced capacities in comparison to more complex, wet chemistry-based synthesis routes. In contrast these more complex approaches, which typically aim at intercalating the Si phases between the individual layers of the rGO matrix, we use a simpler, layer-based spray-coating approach, which is much easier to scale up. In this context, the carbon matrix rGO serves as a mediator for the electrical and ionic conductivity into the silicon interlayers consisting of nm-sized particles. According to the XPS analysis the functional groups of LiPAA binder interact more strongly with the surface groups of rGO and Si, thus enabling sufficient adhesion and - in combination with the high flexibility provided by the polymer backbone - mitigating degradation due to delamination.

The number of silicon interlayers was varied (1, 2 and 3 Si interlayers) with a weight proportion of 14 or 17 wt.% silicon in order to maintain a constant Si content, which resulted in a reduction in layer thickness on the one hand and an increase in the Si surface exposed to the electrolyte on the other. The results demonstrate that reducing the layer thickness from 8 μm to 3.5 μm to 2.2 μm increases capacity by approximately 40 %. It was also found that the limiting factor in this case was not, as initially assumed, the poor CE of the first cycles due to increased formation of SEI. Instead, the reduction in capacity was determined to be a consequence of the morphological change in the silicon layer, which resulted in a reduced electrochemical accessibility, as evidenced by the SEM/EDS and differential capacity analysis. The thickness ratio of the carbon to silicon layer is a fundamental challenge for the stability of this alternating layer electrodes. Therefore, the silicon content was increased from 14 to 26 to 39 wt.% Si, with a constant number of three intermediate silicon layers resulting in a proportional increase in layer thickness. The EIS and GITT measurements indicated an increase in resistivity and a decrease in Li$^+$ diffusivity, corresponding to a decrease in the overall electrochemical accessibility of silicon within the entire electrode. The combination of an increased diffusion path length and an overall lower electrode conductivity resulted in a significant decrease in the utilization of the theoretical maximum electrode capacity. The accessibility (ζ) reaches a minimum with a decreasing carbon to silicon layer ratio ($\zeta_{c39wt.\% Si} = 39 \% < \zeta_{c26wt.\% Si} = 62 \% < \zeta_{c14wt.\% Si} = 95 \%$).

Furthermore, a Si interlayer thickness > 7 μm, leads to a strong but regularly recurring fluctuation in the de/lithiation capacity, observed during cycling. The extended post-mortem analysis of the cross-sections with SEM/EDS, XRD and light microscopy revealed that the microstructure of the interlayers underwent a significant transformation. The rGO interlayers were observed to be displaced, resulting in the formation of an area of reduced electrochemical accessibility, which consisted of already passivated, amorphous and uncycled, crystalline silicon. The voltage-resolved, differential capacity analysis indicated that the capacity repetitive fluctuations are attributed to a periodic activation of not yet cycled, crystalline silicon and its subsequent deactivation. Due to the results obtained from the initial GITT measurements, it can be concluded that this effect can be suppressed with a silicon layer thickness limitation. The potential impact of a an alternating thin-layer strategy has been validated up to a layer number of three; however, possible side effects on the performance of electrodes with layers ≥ 4 remain to be confirmed.

Our findings collectively illustrate that the integration of layered SirGO electrodes comprising a substantial number of thin silicon interlayers represents a promising strategy to achieve capacities of up to 840 mAh g^{-1}, with a utilization rate of more than 95 %.

Funding sources

CRediT authorship contribution statement

Tilo Held: Writing – original draft, Visualization, Validation, Software, Methodology, Investigation, Formal analysis, Data curation, Conceptualization. **Wiebke Hagemeier:** Writing – original draft, Visualization, Validation, Methodology, Investigation, Formal analysis, Data curation, Conceptualization. **Daniel Leykam:** Writing – review & editing, Supervision, Software, Formal analysis, Data curation. **Christina Roth:** Writing – review & editing, Supervision, Resources, Funding acquisition, Conceptualization.

Declaration of competing interest

The authors declare that they have no known competing financial interests or personal relationships that could have appeared to influence the work reported in this paper.

Acknowledgments

Supplementary materials

Supplementary material associated with this article can be found, in the online version, at doi:10.1016/j.electacta.2025.146123.

Data availability

Data will be made available on request.

References

[1] J.M. Tarascon, M. Armand, Issues and challenges facing rechargeable lithium batteries, Nature 414 (2001) 359–367, https://doi.org/10.1038/35104644.

[2] M.N. Obrovac, L. Christensen, Structural changes in silicon anodes during lithium insertion/extraction, Electrochem. Solid State Lett. 7 (2004) A93, https://doi.org/10.1149/1.1652421.

[3] E.H. Putley, W.H. Mitchell, The electrical conductivity and hall effect of silicon, Proc. Phys. Soc. 72 (1958) 193–200, https://doi.org/10.1088/0370-1328/72/2/303.

[4] M. Weiss, R. Ruess, J. Kasnatscheew, Y. Levartovsky, N.R. Levy, P. Minnmann, L. Stolz, T. Waldmann, M. Wohlfahrt-Mehrens, D. Aurbach, M. Winter, Y. Ein-Eli, J. Janek, Fast charging of lithium-ion batteries: a review of materials aspects, Adv. Energy Mater. 11 (2021) 2101126, https://doi.org/10.1002/aenm.202101126.

[5] F. Dou, L. Shi, G. Chen, D. Zhang, Silicon/carbon composite anode materials for lithium-ion batteries, Electrochem. Energy Rev. 2 (2019) 149–198, https://doi.org/10.1007/s41918-018-00028-w.

[6] M. Graf, C. Berg, R. Bernhard, S. Haufe, J. Pfeiffer, H.A. Gasteiger, Effect and progress of the amorphization process for microscale silicon particles under partial lithiation as active material in lithium-ion batteries, J. Electrochem. Soc. 169 (2022) 20536, https://doi.org/10.1149/1945-7111/ac4b80.

[7] F. Tariq, V. Yufit, D.S. Eastwood, Y. Merla, M. Biton, B. Wu, Z. Chen, K. Freedman, G. Offer, E. Peled, P.D. Lee, D. Golodnitsky, N. Brandon, In-operando X-ray tomography study of lithiation induced delamination of Si based anodes for lithium-ion batteries, ECS Electrochemistry Letters 3 (2014) A76–A78, https://doi.org/10.1149/2.0081407eel.

[8] C. Zhao, T. Wada, V. de Andrade, D. Gürsoy, H. Kato, Y.K. Chen-Wiegart, Imaging of 3D morphological evolution of nanoporous silicon anode in lithium ion battery by X-ray nano-tomography, Nano Energy 52 (2018) 381–390, https://doi.org/10.1016/j.nanoen.2018.08.009.

[9] S. Poetke, S. Cangaz, F. Hippauf, S. Haufe, S. Dörfler, H. Althues, S. Kaskel, Partially lithiated microscale silicon particles as anode material for high-energy solid-state lithium-ion batteries, Energy Tech 11 (2023) 2201330, https://doi.org/10.1002/ente.202201330.

[10] N. Kirkaldy, M.A. Samieian, G.J. Offer, M. Marinescu, Y. Patel, Lithium-ion battery degradation: measuring rapid loss of active silicon in silicon-graphite composite electrodes, ACS Appl. Energy Mater. 5 (2022) 13367–13376, https://doi.org/10.1021/acsaem.2c02047.

[11] X.H. Liu, L. Zhong, S. Huang, S.X. Mao, T. Zhu, J.Y. Huang, Size-dependent fracture of silicon nanoparticles during lithiation, ACS Nano 6 (2012) 1522–1531, https://doi.org/10.1021/nn204476h.

[12] A. Amin, M. Loewenich, S.O. Kilian, T. Wassmer, S. Bade, J. Lyubina, H. Wiggers, F. Özcan, D. Segets, One-step non-reactive spray drying approach to produce silicon/carbon composite-based hierarchically structured suprapaticles for lithium-ion battery anodes, J. Electrochem. Soc. 170 (2023) 20523, https://doi.org/10.1149/1945-7111/acb66b.

[13] S. Müllner, T. Held, A. Schmidt-Rodenkirchen, T. Gerdes, C. Roth, Reactive spray drying as a one-step synthesis approach towards Si/rGO anode materials for lithium-ion batteries, J. Electrochem. Soc. 168 (2021) 120545, https://doi.org/10.1149/1945-7111/ac429d.

[14] H. Jia, J. Zheng, J. Song, L. Luo, R. Yi, L. Estevez, W. Zhao, R. Patel, X. Li, J. G. Zhang, A novel approach to synthesize micrometer-sized porous silicon as a high performance anode for lithium-ion batteries, Nano Energy 50 (2018) 589–597, https://doi.org/10.1016/j.nanoen.2018.05.048.

[15] M. Tokur, M.Y. Jin, B.W. Sheldon, H. Akbulut, Stress bearing mechanism of reduced graphene oxide in silicon-based composite anodes for lithium ion batteries, ACS Appl. Mater. Interfaces 12 (2020) 33855–33869, https://doi.org/10.1021/acsami.0c10064.

[16] S. Palumbo, L. Silvestri, A. Ansaldo, R. Brescia, F. Bonaccorso, V. Pellegrini, Silicon few-layer graphene nanocomposite as high-capacity and high-rate anode in lithium-ion batteries, ACS Appl. Energy Mater. 2 (2019) 1793–1802, https://doi.org/10.1021/acsaem.8b01927.

[17] H. Zhou, J. Zhang, J. Liu, S. Feng, C. Li, E. Marsili, X. Zhang, Silicon nanospheres supported on conductive MXene nanosheets as anodes for lithium-ion batteries, ACS Appl. Energy Mater. 6 (2023) 160–169, https://doi.org/10.1021/acsaem.2c02706.

[18] J. Kim, O.B. Chae, B.L. Lucht, Perspective—structure and stability of the solid electrolyte interphase on silicon anodes of lithium-ion batteries, J. Electrochem. Soc. 168 (2021) 30521, https://doi.org/10.1149/1945-7111/abe984.

[19] M. Nie, D. Chalasani, D.P. Abraham, Y. Chen, A. Bose, B.L. Lucht, Lithium ion battery graphite solid electrolyte interphase revealed by microscopy and spectroscopy, J. Phys. Chem. C 117 (2013) 1257–1267, https://doi.org/10.1021/jp3118055.

[20] E. Evshchik, D. Novikov, A. Levchenko, S. Nefedkin, A.V. Shikhovtseva, O. V. Bushkova, Y.A. Dobrovolsky, Magnetron sputtering silicon thin film electrodes for lithium-ion batteries, Int. J. Electrochem. Sci. 13 (2018) 2860–2874, https://doi.org/10.20964/2018.03.05.

[21] A.Reyes Jiménez, R. Klöpsch, R. Wagner, U.C. Rodehorst, M. Kolek, R. Nölle, M. Winter, T. Placke, A step toward high-energy silicon-based thin film lithium ion batteries, ACS Nano 11 (2017) 4731–4744, https://doi.org/10.1021/acsnano.7b00922.

[22] L. Chai, X. Wang, C. Bi, B. Su, C. Zhang, X. Li, W. Xue, Lifetime optimization of amorphous silicon thin-film anodes for lithium-ion batteries, ACS Appl. Energy Mater. 6 (2023) 8388–8396, https://doi.org/10.1021/acsaem.3c01127.

[23] R.Y. Azeemi, R. Ergün, A. Taşdemir, S. Alkan Gürsel, A. Yürüm, A simple spray assisted method to fabricate high performance layered graphene/silicon hybrid anodes for lithium-ion batteries, Int. J. Hydrog. Energy 44 (2019) 20267–20277, https://doi.org/10.1016/j.ijhydene.2019.05.200.

[24] P.K. Lee, T. Tan, S. Wang, W. Kang, C.S. Lee, D.Y.W. Yu, Robust micron-sized silicon secondary particles anchored by polyimide as high-capacity, high-stability li-ion battery anode, ACS Appl. Mater. Interfaces 10 (2018) 34132–34139, https://doi.org/10.1021/acsami.8b09566.

[25] L. Tong, P. Wang, W. Fang, X. Guo, W. Bao, Y. Yang, S. Shen, F. Qiu, Interface engineering of silicon/carbon thin-film anodes for high-rate lithium-ion batteries, ACS Appl. Mater. Interfaces 12 (2020) 29242–29252, https://doi.org/10.1021/acsami.0c05140.

[26] C. Ni, C. Xia, W. Liu, W. Xu, Z. Shan, X. Lei, H. Qin, Z. Tao, Effect of graphene on the performance of silicon-carbon composite anode materials for lithium-ion batteries, Materials (2024) 17, https://doi.org/10.3390/ma17030754. . (Basel).

[27] J. Peng, G. Ji, X. Wang, Cycling performance and failure behavior of lithium-ion battery silicon-carbon composite electrode, J. Electroanal. Chem. 956 (2024) 118095, https://doi.org/10.1016/j.jelechem.2024.118095.

[28] L.d Santos-Gómez, N. Cuesta, I. Cameán, A.B. García, A. Arenillas, A promising silicon/carbon xerogel composite for high-rate and high-capacity lithium-ion batteries, Electrochim. Acta 426 (2022) 140790, https://doi.org/10.1016/j.electacta.2022.140790.

[29] Y. Yang, R. Zhang, Q. Zhang, L. Feng, G. Wen, L.C. Qin, D. Wang, Using sandwiched silicon/reduced graphene oxide composites with dual hybridization for their stable lithium storage properties, Molecules 29 (2024), https://doi.org/10.3390/molecules29102178.

[30] C. Huang, A. Kim, D.J. Chung, E. Park, N.P. Young, K. Jurkschat, H. Kim, P. S. Grant, Multiscale engineered Si/SiO x nanocomposite electrodes for lithium-ion batteries using layer-by-layer spray deposition, ACS Appl. Mater. Interfaces 10 (2018) 15624–15633, https://doi.org/10.1021/acsami.8b00370.

[31] B. Han, M.J. Piernas-Muñoz, F. Dogan, J. Kubal, S.E. Trask, I.D. Bloom, J. T. Vaughey, B. Key, Probing the reaction between PVDF and LiPAA vs Li 7 Si 3

[31] investigation of binder stability for Si anodes, J. Electrochem. Soc. 166 (2019) A2396–A2402, https://doi.org/10.1149/2.0241912jes.

[32] D.H. Yoon, M. Marinaro, P. Axmann, M. Wohlfahrt-Mehrens, Study of the binder influence on expansion/contraction behavior of silicon alloy negative electrodes for lithium-ion batteries, J. Electrochem. Soc. 167 (2020) 160537, https://doi.org/10.1149/1945-7111/abcf4f.

[33] W. Porcher, S. Chazelle, A. Boulineau, N. Mariage, J.P. Alper, T. van Rompaey, J. S. Bridel, C. Haon, Understanding polyacrylic acid and lithium polyacrylate binder behavior in silicon based electrodes for li-ion batteries, J. Electrochem. Soc. 164 (2017) A3633–A3640, https://doi.org/10.1149/2.0821714jes.

[34] K.A. Hays, R.E. Ruther, A.J. Kukay, P. Cao, T. Saito, D.L. Wood, J. Li, What makes lithium substituted polyacrylic acid a better binder than polyacrylic acid for silicon-graphite composite anodes? J. Power Sources. 384 (2018) 136–144, https://doi.org/10.1016/j.jpowsour.2018.02.085.

[35] H. Tao, L. Xiong, S. Zhu, L. Zhang, X. Yang, Porous Si/C/reduced graphene oxide microspheres by spray drying as anode for Li-ion batteries, J. Electroanal. Chem. 797 (2017) 16–22, https://doi.org/10.1016/j.jelechem.2017.05.010.

[36] S. Müllner, T. Michlik, M. Reichel, T. Held, R. Moos, C. Roth, Effect of water-soluble CMC/SBR binder ratios on Si-rGO composites using μM- and nm-sized silicon as anode materials for lithium-ion batteries, Batteries 9 (2023) 248, https://doi.org/10.3390/batteries9050248. . (Basel).

[37] S. Müllner, T. Held, T. Tichter, P. Rank, D. Leykam, W. Jiang, T. Lunkenbein, T. Gerdes, C. Roth, Impact of functional groups in reduced graphene oxide matrices for high energy anodes in lithium-ion batteries, J. Electrochem. Soc. 170 (2023) 70523, https://doi.org/10.1149/1945-7111/ace70a.

[38] N. Lingappan, L. Kong, M. Pecht, The significance of aqueous binders in lithium-ion batteries, Renew. Sustain. Energy Rev. 147 (2021) 111227, https://doi.org/10.1016/j.rser.2021.111227.

[39] N.S. Hochgatterer, M.R. Schweiger, S. Koller, P.R. Raimann, T. Wöhrle, C. Wurm, M. Winter, Silicon/graphite composite electrodes for high-capacity anodes: influence of binder chemistry on cycling stability, Electrochem. Solid State Lett. 11 (2008) A76, https://doi.org/10.1149/1.2888173.

[40] S. Komaba, K. Okushi, T. Ozeki, H. Yui, Y. Katayama, T. Miura, T. Saito, H. Groult, Polyacrylate modifier for graphite anode of lithium-ion batteries, Electrochem. Solid State Lett. 12 (2009) A107, https://doi.org/10.1149/1.3086262.

[41] P. Parikh, M. Sina, A. Banerjee, X. Wang, M.S. D'Souza, J.M. Doux, E.A. Wu, O. Y. Trieu, Y. Gong, Q. Zhou, K. Snyder, Y.S. Meng, Role of polyacrylic acid (PAA) binder on the solid electrolyte interphase in silicon anodes, Chem. Mater. 31 (2019) 2535–2544, https://doi.org/10.1021/acs.chemmater.8b05020.

[42] Z. Karkar, D. Guyomard, L. Roué, B. Lestriez, A comparative study of polyacrylic acid (PAA) and carboxymethyl cellulose (CMC) binders for Si-based electrodes, Electrochim. Acta 258 (2017) 453–466, https://doi.org/10.1016/j.electacta.2017.11.082.

[43] T.B. Truong, Y.R. Chen, G.Y. Lin, H.T. Lin, Y.S. Wu, C.C. Yang, Lithium polyacrylate polymer coating enhances the performance of graphite/silicon/carbon composite anodes, Electrochim. Acta 365 (2021) 137387, https://doi.org/10.1016/j.electacta.2020.137387.

[44] J. Xiong, N. Dupré, D. Mazouzi, D. Guyomard, L. Roué, B. Lestriez, Influence of the polyacrylic acid binder neutralization degree on the initial electrochemical behavior of a silicon/graphite electrode, ACS Appl. Mater. Interfaces 13 (2021) 28304–28323, https://doi.org/10.1021/acsami.1c06683.

[45] M. Wetjen, D. Pritzl, R. Jung, S. Solchenbach, R. Ghadimi, H.A. Gasteiger, Differentiating the degradation phenomena in silicon-graphite electrodes for lithium-ion batteries, J. Electrochem. Soc. 164 (2017) A2840–A2852, https://doi.org/10.1149/2.1921712jes.

[46] S.Y. Lai, K.D. Knudsen, B.T. Sejersted, A. Ulvestad, J.P. Mæhlen, A.Y. Koposov, Silicon nanoparticle ensembles for lithium-ion batteries elucidated by small-angle neutron scattering, ACS Appl. Energy Mater. 2 (2019) 3220–3227, https://doi.org/10.1021/acsaem.9b00071.

[47] J. Piwowarczyk, R. Jędrzejewski, D. Moszyński, K. Kwiatkowski, A. Niemczyk, J. Baranowska, XPS and FTIR studies of polytetrafluoroethylene thin films obtained by physical methods, Polymers 11 (2019), https://doi.org/10.3390/polym11101629. . (Basel).

[48] R.E. Ruther, K.A. Hays, S.J. An, J. Li, D.L. Wood, J. Nanda, Chemical evolution in silicon-graphite composite anodes investigated by vibrational spectroscopy, ACS Appl. Mater. Interfaces 10 (2018) 18641–18649, https://doi.org/10.1021/acsami.8b02197.

[49] D. Pantea, H. Darmstadt, S. Kaliaguine, C. Roy, Electrical conductivity of conductive carbon blacks: influence of surface chemistry and topology, Appl. Surf. Sci. 217 (2003) 181–193, https://doi.org/10.1016/S0169-4332(03)00550-6.

[50] D. Yang, A. Velamakanni, G. Bozoklu, S. Park, M. Stoller, R.D. Piner, S. Stankovich, I. Jung, D.A. Field, C.A. Ventrice, R.S. Ruoff, Chemical analysis of graphene oxide films after heat and chemical treatments by X-ray photoelectron and Micro-Raman spectroscopy, Carbon 47 (2009) 145–152, https://doi.org/10.1016/j.carbon.2008.09.045. . N. Y.

[51] D. Yoon, K.Y. Chung, W. Chang, S.M. Kim, M.J. Lee, Z. Lee, J. Kim, Hydrogen-enriched reduced graphene oxide with enhanced electrochemical performance in lithium ion batteries, Chem. Mater. 27 (2015) 266–275, https://doi.org/10.1021/cm503861r.

[52] F. Jeschull, H.Q. Pham, A. Ghamlouche, P.K. Thakur, S. Trabesinger, J. Maibach, Interphase formation with carboxylic acids as slurry additives for Si electrodes in Li-ion batteries. Part 2: a photoelectron spectroscopy study, J. Phys. Energy 5 (2023) 25002, https://doi.org/10.1088/2515-7655/acbbee.

[53] B. Philippe, R. Dedryvère, J. Allouche, F. Lindgren, M. Gorgoi, H. Rensmo, D. Gonbeau, K. Edström, Nanosilicon electrodes for lithium-ion batteries:

interfacial mechanisms studied by hard and soft x-ray photoelectron spectroscopy, Chem. Mater. 24 (2012) 1107–1115, https://doi.org/10.1021/cm2034195.

[54] M.K. Burdette-Trofimov, B.L. Armstrong, A.M. Rogers, L. Heroux, M. Doucet, G. Yang, N.D. Phillip, M.K. Kidder, G.M. Veith, Understanding binder–silicon interactions during slurry processing, J. Phys. Chem. C 124 (2020) 13479–13494, https://doi.org/10.1021/acs.jpcc.0c03660.

[55] S. Jiang, B. Hu, R. Sahore, L. Zhang, H. Liu, L. Zhang, W. Lu, B. Zhao, Z. Zhang, Surface-functionalized silicon nanoparticles as anode material for lithium-ion battery, ACS Appl. Mater. Interfaces 10 (2018) 44924–44931, https://doi.org/10.1021/acsami.8b17729.

[56] S.E. Trask, K.Z. Pupek, J.A. Gilbert, M. Klett, B.J. Polzin, A.N. Jansen, D. P. Abraham, Performance of full cells containing carbonate-based LiFSI electrolytes and silicon-graphite negative electrodes, J. Electrochem. Soc. 163 (2016) A345–A350, https://doi.org/10.1149/2.0981602jes.

[57] W. Bao, C. Fang, D. Cheng, Y. Zhang, B. Lu, D.H. Tan, R. Shimizu, B. Sreenarayanan, S. Bai, W. Li, M. Zhang, Y.S. Meng, Quantifying lithium loss in amorphous silicon thin-film anodes via titration-gas chromatography, Cell Rep. Phys. Sci. 2 (2021) 100597, https://doi.org/10.1016/j.xcrp.2021.100597.

[58] Y. Li, X. Zheng, Z. Cao, Y. Wang, Y. Wang, L. Lv, W. Huang, Y. Huang, H. Zheng, Unveiling the mechanisms into Li-trapping induced (ir)reversible capacity loss for silicon anode, Energy Storage Mater. 55 (2023) 660–668, https://doi.org/10.1016/j.ensm.2022.12.032.

[59] J. Kim, H. Jeong, E. Oh, J. Jang, S.W. Lee, D.H. Kim, S.D. Han, J. Kim, J. Yang, Negative effect of the calendering process on the interphase formation and electrochemical behavior of reduced graphene oxide electrodes, ACS Appl. Mater. Interfaces (2024), https://doi.org/10.1021/acsami.4c09721.

[60] A.L. Michan, M. Leskes, C.P. Grey, Voltage dependent solid electrolyte interphase formation in silicon electrodes: monitoring the formation of organic decomposition products, Chem. Mater. 28 (2016) 385–398, https://doi.org/10.1021/acs.chemmater.5b04408.

[61] J. Li, J.R. Dahn, An *in situ* X-ray diffraction study of the reaction of Li with crystalline Si, J. Electrochem. Soc. 154 (2007) A156, https://doi.org/10.1149/1.2409862.

[62] M.N. Obrovac, L.J. Krause, Reversible cycling of crystalline silicon powder, J. Electrochem. Soc. 154 (2007) A103, https://doi.org/10.1149/1.2402112.

[63] J.H. Park, J. Ku, J.W. Lim, J. Choi, I.H. Son, Adhesive interlayer between active film and current collector for improving the performance of silicon anodes of Li-ion batteries, J. Electroanal. Chem. 778 (2016) 53–56, https://doi.org/10.1016/j.jelechem.2016.08.015.

[64] N. Ding, J. Xu, Y.X. Yao, G. Wegner, X. Fang, C.H. Chen, I. Lieberwirth, Determination of the diffusion coefficient of lithium ions in nano-Si, Solid State Ion. 180 (2009) 222–225, https://doi.org/10.1016/j.ssi.2008.12.015.

[65] G. Hua-jun, L. Xin-hai, Z. Xin-ming, W. Hong-qiang, W. Zhi-xing, P. Wen-jie, Diffusion coefficient of lithium in artificial graphite, mesocarbon microbeads, and disordered carbon, New Carbon Mater. 22 (2007) 7–10, https://doi.org/10.1016/S1872-5805(07)60006-7.

[66] J. Guo, A. Sun, X. Chen, C. Wang, A. Manivannan, Cyclability study of silicon–carbon composite anodes for lithium-ion batteries using electrochemical impedance spectroscopy, Electrochim. Acta 56 (2011) 3981–3987, https://doi.org/10.1016/j.electacta.2011.02.014.

[67] C. Li, T. Shi, D. Li, H. Yoshitake, H. Wang, Effect of surface modification on electrochemical performance of nano-sized Si as an anode material for Li-ion batteries, RSC Adv. 6 (2016) 34715–34723, https://doi.org/10.1039/C5RA28021D.

[68] T. Yim, S.J. Choi, Y.N. Jo, T.H. Kim, K.J. Kim, G. Jeong, Y.J. Kim, Effect of binder properties on electrochemical performance for silicon-graphite anode: Method and application of binder screening, Electrochim. Acta 136 (2014) 112–120, https://doi.org/10.1016/j.electacta.2014.05.062.

[69] D. Martín-Yerga, D.C. Milan, X. Xu, J. Fernández-Vidal, L. Whalley, A.J. Cowan, L. J. Hardwick, P.R. Unwin, Dynamics of solid-electrolyte interphase formation on silicon electrodes revealed by combinatorial electrochemical screening, Angew. Chem. Int. Ed. Engl. 61 (2022) e202207184, https://doi.org/10.1002/anie.202207184.

[70] J. Kaspar, M. Graczyk-Zajac, R. Riedel, Determination of the chemical diffusion coefficient of Li-ions in carbon-rich silicon oxycarbide anodes by electro-analytical methods, Electrochim. Acta 115 (2014) 665–670, https://doi.org/10.1016/j.electacta.2013.10.184.

[71] C.J. Wen, B.A. Boukamp, R.A. Huggins, W. Weppner, Thermodynamic and mass transport properties of " LiAl", J. Electrochem. Soc. 126 (1979) 2258–2266, https://doi.org/10.1149/1.2128939.

[72] H. Zhang, P. Zong, M. Chen, H. Jin, Y. Bai, S. Li, F. Ma, K. Xu, K. Lian, *In situ* synthesis of multilayer carbon matrix decorated with copper particles: enhancing the performance of Si as anode for Li-ion batteries, ACS Nano 13 (2019) 3054–3062, https://doi.org/10.1021/acsnano.8b08088.

[73] T.L. Kulova, A.M. Skundin, Y. Pleskov, E.I. Terukov, O.I. Kon'kov, Lithium insertion into amorphous silicon thin-film electrodes, J. Electroanal. Chem. 600 (2007) 217–225, https://doi.org/10.1016/j.jelechem.2006.07.002.

[74] K. Persson, V.A. Sethuraman, L.J. Hardwick, Y. Hinuma, Y.S. Meng, A. van der Ven, V. Srinivasan, R. Kostecki, G. Ceder, Lithium diffusion in graphitic carbon, J. Phys. Chem. Lett. 1 (2010) 1176–1180, https://doi.org/10.1021/jz100188d.

[75] Z. Wang, Z. Mu, T. Ma, W. Yan, D. Wu, M. Yang, J. Peng, Y. Xia, S. Shi, L. Chen, H. Li, F. Wu, Soft carbon-thiourea with fast bulk diffusion kinetics for solid-state lithium metal batteries, Adv. Mater. 36 (2024) e2310395, https://doi.org/10.1002/adma.202310395.

[76] Y. Joshi, A. Umasankaran, C. Klaassen, M. AlAmer, Y.L. Joo, Critical roles of reduced graphene oxide in the electrochemical performance of silicon/reduced graphene oxide hybrids for high rate capable lithium-ion battery anodes, Electrochim. Acta 404 (2022) 139753, https://doi.org/10.1016/j.electacta.2021.139753.

[77] S.P. Nadimpalli, V.A. Sethuraman, S. Dalavi, B. Lucht, M.J. Chon, V.B. Shenoy, P. R. Guduru, Quantifying capacity loss due to solid-electrolyte-interphase layer formation on silicon negative electrodes in lithium-ion batteries, J. Power Sources 215 (2012) 145–151, https://doi.org/10.1016/j.jpowsour.2012.05.004.

[78] Y. Jiang, G. Offer, J. Jiang, M. Marinescu, H. Wang, Voltage hysteresis model for silicon electrodes for lithium ion batteries, including multi-step phase transformations, crystallization and amorphization, J. Electrochem. Soc. 167 (2020) 130533, https://doi.org/10.1149/1945-7111/abbbba.

[79] S.N. Alam, N. Sharma, L. Kumar, Synthesis of graphene oxide (GO) by modified hummers method and its thermal reduction to obtain reduced graphene oxide (rGO)*, Graphene 06 (2017) 1–18, https://doi.org/10.4236/graphene.2017.61001.

[80] X.H. Yau, F.W. Low, C.S. Khe, C.W. Lai, S.K. Tiong, N. Amin, An investigation of the stirring duration effect on synthesized graphene oxide for dye-sensitized solar cells, PLoS One 15 (2020) e0228322, https://doi.org/10.1371/journal.pone.0228322.

[81] A.Y. Kharin, Y.V. Kargina, V.Y. Timoshenko, Evolution of nanocrystal size distribution in porous silicon nanoparticles during storage in aqueous media: X-ray diffraction analysis, J. Nanoparticle Res. 21 (2019), https://doi.org/10.1007/s11051-019-4466-9.

[82] J.K. Lee, K.B. Smith, C.M. Hayner, H.H. Kung, Silicon nanoparticles-graphene paper composites for Li ion battery anodes, Chem. Commun. 46 (2010) 2025–2027, https://doi.org/10.1039/b919738a (Camb).

[83] E.A. Owen, E.L. Yates, Precision measurements of crystal parameters, Philos. Mag. 15 (1933) 472–488. , Serie 7(1926-46,1955).

[84] H. Effenberger, J. Zemann, Verfeinerung der Kristallstruktur des Lithiumkarbonates, Li2C03, Z. Krist. Cryst. Mater. 150 (1979) 133–138, https://doi.org/10.1524/zkri.1979.150.14.133.

[85] Y. Idemoto, J.W. Richardson, N. Koura, S. Kohara, C.K. Loong, Crystal structure of (LiXK1 −x) 2CO3 (x = 0, 0.43, 0.5, 0.62, 1) by neutron powder diffraction analysis, J. Phys. Chem. Solids 59 (1998) 363–376, https://doi.org/10.1016/S0022-3697(97)00209-6.

[86] M. Schellenberger, R. Golnak, W.G. Quevedo Garzon, S. Risse, R. Seidel, Accessing the solid electrolyte interphase on silicon anodes for lithium-ion batteries *in-situ* through transmission soft X-ray absorption spectroscopy, Mater. Today Adv. 14 (2022) 100215, https://doi.org/10.1016/j.mtadv.2022.100215.

[87] C. Gan, X. Ye, S. Zhang, J. Chen, W. Wen, Y. Liu, D.L. Peng, L. Tang, X. Luo, Current density induced growth of Li15Si4 alloy in silicon-carbon anodes during first lithiation process, J. Energy Storage 41 (2021) 102930, https://doi.org/10.1016/j.est.2021.102930.

[88] X. Ji, N.J. Fritz, H. Jeong, P. Lu, J.W. Lin, P.V. Braun, D.G. Cahill, Lithium trapping, hydrogen content, and solid electrolyte interphase growth in electrodeposited silicon anodes by ion beam analysis, J. Power Sources 614 (2024) 235039, https://doi.org/10.1016/j.jpowsour.2024.235039.

[89] A. Saidi, A. Tanguy, M. Fourmeau, G. Molnár, A. Boucherif, D. Machon, Coupling between mechanical stresses and lithium penetration in a lithium ion battery, Mech. Mater. 177 (2023) 104532, https://doi.org/10.1016/j.mechmat.2022.104532.

[90] Y. Suo, H. Yang, Q. Jia, Coupled diffusion-mechanical analysis with dislocation effect in porous spherical electrode, Solid State Ion. 404 (2024) 116422, https://doi.org/10.1016/j.ssi.2023.116422.

[91] A.Y.R. Prado, M.T.F. Rodrigues, S.E. Trask, L. Shaw, D.P. Abraham, Electrochemical dilatometry of si-bearing electrodes: dimensional changes and experiment design, J. Electrochem. Soc. 167 (2020) 160551, https://doi.org/10.1149/1945-7111/abd465.

[92] J. Peng, G. Ji, X. Wang, Investigating the effects of silicon and carbon components on the thickness evolution and performance degradation of silicon–carbon electrodes through electrochemical dilatometry, J. Power Sources 608 (2024) 234626, https://doi.org/10.1016/j.jpowsour.2024.234626.

[93] I. Dienwiebel, M. Winter, M. Börner, Visualization of degradation mechanisms of negative electrodes based on silicon nanoparticles in lithium-ion batteries via quasi *in situ* scanning electron microscopy and energy-dispersive X-ray spectroscopy, J. Phys. Chem. C 126 (2022) 11016–11025, https://doi.org/10.1021/acs.jpcc.2c03294.